Tuning Critical Field, Critical Current, and Diode Effect of Narrow Thin-Film Superconductors Through Engineering Inhomogeneous Pearl Length

Takayuki Kubo[1,2,*]

[1]*High Energy Accelerator Research Organization (KEK), Tsukuba, Ibaraki 305-0801, Japan*
[2]*The Graduate University for Advanced Studies (Sokendai), Hayama, Kanagawa 240-0193, Japan*

We explore critical field and critical current behavior in inhomogeneous narrow thin-film superconducting strips. Formulations are developed to calculate free energy, critical field, and critical current for strips with inhomogeneous Pearl-length distributions. Our findings show that inhomogeneities, specifically a shorter Pearl length in the middle of the strip, significantly enhance the critical field B_{c1}. This has practical implications for achieving complete flux expulsion. While narrow strips have traditionally been considered the most effective approach to improve B_{c1} and eliminate trapped vortices, our results suggest that engineered inhomogeneities offer an alternative method to enhance the critical field and improve flux expulsion without reducing strip width, providing greater design flexibility for superconducting devices. Additionally, we find that for the purpose of increasing the critical current, utilizing an inhomogeneous film with a reduced Pearl length in the middle of the strip is advantageous. The enhancement in critical current arises from the current suppression effect at the edges induced by the inhomogeneous distribution of superfluid density. Furthermore, we demonstrate that an inhomogeneous film with a left-right asymmetric Pearl-length distribution enables control over the nonreciprocity of the critical current, highlighting the potential of engineering inhomogeneous Pearl-length distributions to implement devices exhibiting the superconducting diode effect. Our results provide concrete examples of how manipulating the inhomogeneity of Pearl length can enhance the performance of superconducting devices. Various methods such as doping nonuniform impurities or creating a temperature gradient can be employed to implement an inhomogeneous Pearl-length distribution.

I. INTRODUCTION

Engineering materials with an inhomogeneous structure, such as optimized impurity profiles and heterostructures, has the potential to enhance the performance of various superconducting devices, including superconducting qubits [1], astrophysics detectors [2–4], and particle accelerators [5,6]. Researchers in the field of superconducting resonators for particle accelerators have actively explored different techniques to optimize impurity-diffusion profiles and improve the overall performance of cavity resonators. Notably, the development of impurity doping techniques in the 2010s [7–12], along with the recent introduction of medium temperature baking [13–18], has yielded remarkable advancements, resulting in high-quality factors ranging from approximately 10^{11} to 10^{12}. Furthermore, in the 1990s, the oxygen-diffusion technique based on a combination of low-temperature baking and electropolishing [19–21] demonstrated the capability to achieve large microwave amplitudes near the superheating field [22,23], where the screening current-density approaches the depairing current density [24–29]. Additionally, thin-film heterostructures formed on bulk niobium have been proposed as a means to enhance the achievable microwave amplitudes further [30–36]. Sample tests have demonstrated positive outcomes, validating the effectiveness of the proposed methods [37–43]. Considering these achievements, an intriguing question arises: can we effectively apply these techniques involving inhomogeneous structures to superconducting thin-film devices? To explore this possibility, this paper undertakes a theoretical investigation focusing on a narrow thin-film strip with a large in-plane penetration depth characterized by the Pearl length $\Lambda = 2\lambda^2/d \gg W$ as a representative system (see also Fig. 1). Here, λ represents the London depth, d is the thickness of the film (with $d < \lambda$), and W denotes the width of the strip.

One example that highlights this approach is the enhancement of the critical field in narrow thin-film superconducting strips in the perpendicular magnetic field,

---

*kubotaka@post.kek.jp
Stay-at-home dad on paternity leave for more than 2.5 years, New York, USA.

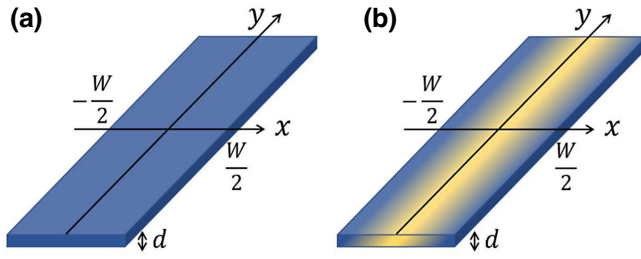034033-1

(a)

(b)

FIG. 1. Schematic illustrations of the geometries investigated in the present study. The difference in color represents the distribution of Pearl length. (a) Homogeneous narrow thin-film strip, and (b) inhomogeneous narrow thin-film strip. The film thickness d and width W satisfy $d < \lambda$ and $W \ll \Lambda$, respectively.

resulting in the complete expulsion of vortices. Trapped vortices contribute to dissipation in superconducting devices, emphasizing the significance of minimizing vortex trapping for improved resonator performance. In homogeneous narrow thin-film strips, vortices are expelled below a nearly material-independent critical field B_{c1} given by $B_{c1} \sim \phi_0/W^2 \ln(W/\xi)$ [44–47], where ϕ_0 is the flux quantum and ξ is the coherence length. Experimental studies have provided evidence consistent with these theoretical observations [45]. Consequently, it has been widely believed that the most practical approach to improve B_{c1} and eliminate trapped vortices is through the design of devices with narrow strips. In this paper, we demonstrate that this strong constraint on B_{c1} is limited to homogeneous films and propose an alternative approach to control B_{c1} without modifying their width. Our method involves engineering the free energy profile through the introduction of an inhomogeneous distribution of the Pearl length, denoted as $\Lambda(x)$. This inhomogeneity can be achieved, for instance, by doping the film with impurities of varying concentrations. Our analysis demonstrates that our proposed method is effective in increasing or decreasing B_{c1} as desired.

Furthermore, our method of engineering the free energy profile provides a means to control the critical current, enabling the implementation of a specific class of superconducting diode effect (SDE) characterized by the unequal disappearance of the vortex energy barrier at the edges [48–50]. This effect is distinct from other SDE mechanisms [51–58]. In the presence of a bias current, the Lorentz force acting on a vortex causes the edge barrier to tilt, allowing vortices to penetrate the thin-film strip once the bias current surpasses the critical value I_c, where the edge barrier vanishes. In homogeneous films, the critical current remains reciprocal when the edge barriers on both sides are equal, regardless of the magnetic field. To achieve a nonreciprocal behavior, it is essential to control the film quality, such as the roughness, at both edges of the film [48–50] (see, e.g., Refs. [59–61] for the impact of roughness on the vortex barrier). On the other hand, in the case

of inhomogeneous films, the nonuniform distribution of the Pearl length $\Lambda(x)$ not only affects the edge barrier but also influences the distribution of the sheet bias current. By engineering an inhomogeneous $\Lambda(x)$, we can design both the edge barrier and the Lorentz force. Through our research, we demonstrate the feasibility of inducing nonreciprocal behavior in the critical current by implementing a left-right asymmetric distribution of $\Lambda(x)$ and applying an external magnetic field.

The paper is organized as follows. In Sec. II, we delve into the investigation of the critical field B_{c1} and its manipulation. We start by examining the established findings in a homogeneous narrow thin-film strip, presented in Sec. II A. This includes the reproduction of well-known results regarding the free energy and B_{c1}. Subsequently, in Sec. II B, we introduce a formulation that allows us to calculate the free energy of an inhomogeneous narrow thin-film strip. We then apply this formulation to a specific problem involving an inhomogeneous $\Lambda(x)$, enabling us to determine the free energy and B_{c1} under such conditions. A noteworthy outcome of this section is the discovery that by engineering an inhomogeneous $\Lambda(x)$, we can effectively increase or decrease the critical field B_{c1}. In Sec. III, our focus shifts towards investigating the influence of an inhomogeneous $\Lambda(x)$ on the critical current. Section III A provides a brief overview of the critical current in homogeneous narrow thin-film strips. In Sec. III B, we formulate the critical current (I_c) calculation for inhomogeneous strips and study the impact of concrete $\Lambda(x)$ distributions. Our study uncovers the potential to achieve nonreciprocal critical currents by implementing left-right asymmetric $\Lambda(x)$ distributions in the presence of an external magnetic field. This discovery opens possibilities for designing devices that exhibit the superconducting diode effect. In Sec. IV, we discuss the implications of our results.

II. CRITICAL FIELD

A. Free energy and critical field in a *homogeneous* narrow thin-film strip

Consider a Pearl vortex in the geometry depicted in Fig. 1(a), which has been extensively studied in the past few decades [44–47,62–68]. In this subsection, we present an alternative approach to reproduce some well-established results from previous studies, which we will utilize in the subsequent subsections to address more complicated cases: inhomogeneous films.

1. Maxwell-London equation for a homogeneous narrow thin-film strip and its solution

Assuming the presence of a single vortex at $\mathbf{r}_v = (X, 0)$, the Maxwell-London (ML) equation governing the behavior of a homogeneous narrow thin-film strip is given by $B + \mu_0 \lambda^2 (\mathrm{rot}\,\mathbf{j})_z = \phi_0 \delta^{(2)}(\mathbf{r} - \mathbf{r}_v)$, where B is the magnetic

field perpendicular to the film, λ is the London depth, $\mathbf{j}$ is the supercurrent density, and ϕ_0 is the flux quantum. Averaging this equation over the z direction yields $B + (1/2)\mu_0\Lambda(\mathrm{rot}\mathbf{J})_z = \phi_0\delta^{(2)}(\mathbf{r} - \mathbf{r}_v)$, where $\mathbf{J} = \int dz\mathbf{j}$ is the sheet current, and $\Lambda = 2\lambda^2/d$ is the Pearl length. Since we consider a narrow film with $W \ll \Lambda$, the second term dominates the left-hand side. Thus, we obtain the following equation:

$$\frac{\mu_0\Lambda}{2}(\mathrm{rot}\mathbf{J})_z = \phi_0\delta^{(2)}(\mathbf{r} - \mathbf{r}_v). \tag{1}$$

The boundary condition is

$$J_x(\pm W/2, y) = 0. \tag{2}$$

We adopt the approach of Kogan [47,63,65,68] and reformulate Eqs. (1) and (2). Because $\mathrm{div}\mathbf{J} = 0$, we can introduce the stream function $\Psi_X(x,y)$, or alternatively, its dimensionless version $\psi_X(x,y) = (\mu_0\Lambda/2\phi_0)\Psi_X(x,y)$, by

$$\mathbf{J} = \mathrm{rot}(\Psi_X\hat{\mathbf{z}}) = \frac{2\phi_0}{\mu_0\Lambda}\mathrm{rot}(\psi_X\hat{\mathbf{z}}) = \frac{2\phi_0}{\mu_0\Lambda}\begin{pmatrix}\partial_y\psi_X \\ -\partial_x\psi_X \\ 0\end{pmatrix}. \tag{3}$$

Here, the subscript X indicates the position of the vortex at $\mathbf{r}_v = (X, 0)$. Then, Eqs. (1) and (2) reduce to

$$-\nabla^2\psi_X(x,y) = \delta^{(2)}(\mathbf{r} - \mathbf{r}_v), \tag{4}$$

$$\psi_X(\pm W/2, y) = 0. \tag{5}$$

The previous studies [63–65,68] have addressed the solutions of Eqs. (4) and (5) through the use of the method of images and conformal mapping. In this section, we present an alternative approach for solving Eqs. (4) and (5) using a more direct method. By employing a Fourier transform of the y coordinate into the k space, we obtain

$$\left(-\frac{\partial^2}{\partial x^2} + k^2\right)\tilde{\psi}_X(x,k) = \delta(x - X), \tag{6}$$

$$\tilde{\psi}_X(\pm W/2, k) = 0. \tag{7}$$

Here,

$$\psi_X(x,y) = \int_{-\infty}^{\infty}\frac{dk}{2\pi}\tilde{\psi}_X(x,k)e^{iky}. \tag{8}$$

Then, Eqs. (6) and (7) are the equation of Green's function for Helmholtz equation in a one-dimensional box, whose solution is given by

$$\tilde{\psi}_X(x,k) = \frac{\cosh k(W - |x - X|) - \cosh k(x + X)}{2k\sinh kW}. \tag{9}$$

Thus, the dimensionless stream function $\psi_X(x,y)$ can be obtained from Eqs. (8) and (9). Notably, the integrand in these equations have poles at $kW = \pm i\pi m$ ($m =$

$1, 2, 3, \ldots$). To evaluate the integrals, we sum the residues at the poles in the upper and lower planes for $y \geq 0$ and $y \leq 0$, respectively. This procedure yields the following expression:

$$\psi_X(x,y) = \frac{1}{2\pi}\sum_{m=1}^{\infty}\frac{(-1)^m}{m}\left[\cos\left\{m\pi\left(1 - \frac{|x - X|}{W}\right)\right\}\right.$$
$$\left. - \cos\left(m\pi\frac{x + X}{W}\right)\right]e^{-m\pi|y|/W}. \tag{10}$$

Although Eq. (10) may appear complex at first glance, it readily reproduces several well-known formulas, as shown below.

2. Self-energy, magnetic moment, and free energy

As derived by Kogan [63,65], the self-energy of a Pearl vortex in a homogeneous thin film is given by

$$\epsilon = \frac{\phi_0}{2}\Psi_X(X_\xi, 0) = \frac{\phi_0^2\psi_X(X_\xi, 0)}{\mu_0\Lambda}. \tag{11}$$

Here, the standard cutoff is applied: $\mathbf{r}_v = (X, 0) \rightarrow (X_\xi, 0)$ and $X_\xi = X + \xi$. It is worthwhile to note that the standard cutoff reflects the limitation of the London theory, where the vortex core is treated as a point singularity. As we approach the core position X, the London theory breaks down, and the cutoff is needed to ensure the validity of the theory outside the core region, where its size is on the order of approximately ξ. In Fourier space, we can express this as

$$\epsilon = \frac{\phi_0^2}{\mu_0\Lambda}\int_{-\infty}^{\infty}\frac{dk}{2\pi}\tilde{\psi}_X(X_\xi, k). \tag{12}$$

Using the formula $\sum_{m=1}^{\infty}(-1)^m\cos(2m\alpha)/m = -\ln 2 - \ln(\cos\alpha)$, we find [46,47,63–66,69]

$$\epsilon = \frac{\phi_0^2}{2\pi\mu_0\Lambda}\ln\frac{\cos(\pi X/W)}{\cos(\pi/2 - \pi\xi/2W)} \tag{13}$$

$$\simeq \frac{\phi_0^2}{2\pi\mu_0\Lambda}\ln\left(\frac{2W}{\pi\xi}\cos\frac{\pi X}{W}\right). \tag{14}$$

The assumption $\xi/W \ll 1$ is utilized in the last line of the equation. Equation (14) represents the well-known formula for the self-energy of a Pearl vortex in a homogeneous narrow thin-film strip. It is worth noting that, in other papers, the strip is often defined over the interval $[0, W]$ rather than our interval of $[-W/2, W/2]$. To obtain the same expression, we must transform $X \rightarrow X + W/2$. Figure 2(a) shows the function ϵ of a vortex (antivortex) positioned at $x = X$.
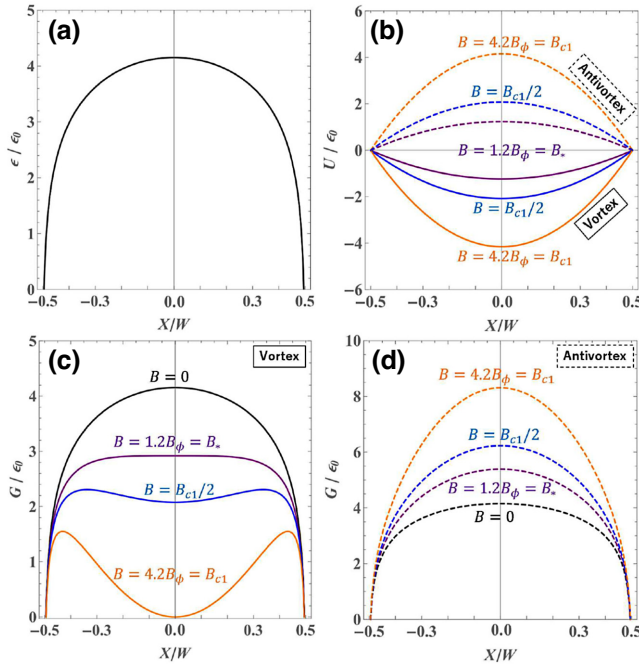
FIG. 2. (a) Self energy ϵ of a vortex or an antivortex as a function of the vortex position $\mathbf{r}_v = (X, 0)$. (b) Magnetic potential $U(X) = -\mu_z B$ for a film with a vortex (solid curve) and an antivortex (dashed curve). (c) Total energy $G(X)$ of a film with a vortex at $x = X$. (d) Total energy $G(X)$ of a film with an antivortex at $x = X$. All calculations in the figures are performed with $\xi/W = 0.01$.

When a vortex exists in the film, it generates a magnetic moment μ_z within the film, which contributes to the magnetic potential $U = -\mu_z B$. The magnetic moment can be calculated from

$$\mu_z(X) = \frac{1}{2} \int d^2 r (\mathbf{r} \times \mathbf{J})_z = \frac{2\phi_0}{\mu_0 \Lambda} \int_{-W/2}^{W/2} dx \, \tilde{\psi}_X(x, 0). \tag{15}$$

Performing a similar calculation for a film containing an antivortex is straightforward. Then, we obtain [46,47,63, 64,66]

$$\mu_z(X) = \pm \frac{\phi_0 W^2}{4\mu_0 \Lambda} \left(1 - \frac{4X^2}{W^2}\right), \tag{16}$$

for a film with a vortex and an antivortex, respectively. It should be noted that, by replacing $X \rightarrow X + W/2$, Eq. (16) can be transformed into the same expression as the papers that consider the strip defined over the interval $[0, W]$. Figure 2(b) illustrates the behavior of $U = -\mu_z B$ when a vortex (antivortex) is situated at $\mathbf{r}_v = (X, 0)$. As B increases (where $B > 0$), $U = -\mu_z B$ is stabilized for a vortex and destabilized for an antivortex.

The free energy of the system in the external magnetic field $\mathbf{B} = (0, 0, B)$ is given by [46,47,63,64,66]

$$
\begin{aligned}
G(X) &= \epsilon(X) - \mu_z(X)B \\
&= \frac{\phi_0^2}{2\pi \mu_0 \Lambda} \ln\left(\frac{2W}{\pi\xi} \cos\frac{\pi X}{W}\right) \mp \frac{\phi_0 W^2 B}{4\mu_0 \Lambda}\left(1 - \frac{4X^2}{W^2}\right),
\end{aligned}
\tag{17}
$$

for a film with a vortex and an antivortex, respectively. Introducing

$$\epsilon_0 = \frac{\phi_0^2}{2\pi \mu_0 \Lambda}, \tag{18}$$

$$B_\phi = \frac{2\phi_0}{\pi W^2}, \tag{19}$$

we have

$$\frac{G(X)}{\epsilon_0} = \ln\left(\frac{2W}{\pi\xi} \cos\frac{\pi X}{W}\right) \mp \frac{B}{B_\phi}\left(1 - 4\frac{X^2}{W^2}\right). \tag{20}$$

Shown in Fig. 2(c) is G for a thin-film strip containing a single vortex. The vortex state is initially unstable at $B = 0$, but becomes stable as B increases. As B exceeds a critical value B_* obtained from the condition $d^2 G/dX^2 = 0$ at $X = 0$, the center of the strip becomes a metastable minimum. Here, B_* is given by $B_* = (\pi^2/8)B_\phi = \pi\phi_0/4W^2$ [45,62], where ϕ_0 is the flux quantum. Further increasing B stabilizes the metastable minimum. At the critical field B_{c1}, which is obtained from the condition $G(0) = 0$, the center of the film becomes the global minimum. B_{c1} is given by [44–47]

$$B_{c1} = B_\phi \ln \frac{2W}{\pi\xi} = \frac{2\phi_0}{\pi W^2} \ln \frac{2W}{\pi\xi}. \tag{21}$$

The edge barrier disappears at the vortex entrance field B_v, which is obtained from the condition $dG/dX = 0$ at the edges. B_v is given by $B_v = (W/4\xi)B_\phi = \phi_0/2\pi\xi W$ [62], but is not shown in Fig. 2. Note here that $B_v \gg \{B_{c1}, B_*\}$ for $\xi/W \ll 1$ (e.g., $B_* = 1.2B_\phi$, $B_{c1} = 4.8B_\phi$, and $B_v = 50B_\phi$ for $\xi/W = 0.005$). On the other hand, G of a film including an antivortex is not stabilized by increasing $B(> 0)$ as shown in Fig. 2(d) but stabilized by $B < 0$.

One of the remarkable properties of a vortex is that the critical field B_{c1} is largely independent of material parameters. For example, reducing the coherence length ξ from $\xi/W = 0.01$ to $\xi/W = 0.005$ by changing the circuit material increases only B_{c1} by a factor of 1.17. Therefore, if one desires to increase B_{c1}, a more realistic option is to decrease the strip width [45] as long as we use a homogeneous film. In the following, it will be demonstrated that this constraint can be avoided by utilizing an inhomogeneous film.

B. Free energy and critical field in an *inhomogeneous narrow thin-film strip*

1. Formulation

Consider the geometry depicted in Fig. 1(b), where Λ is not uniform and depends on x. In this case, Eq. (1) is not applicable, and we must use the following equation (see, e.g., Ref. [70]):

$$\frac{\mu_0}{2}\Big[\mathrm{rot}\{\Lambda(x)\mathbf{J}(\mathbf{r})\}\Big]_z = \phi_0\delta^{(2)}(\mathbf{r}-\mathbf{r_v}). \tag{22}$$

Writing $\Lambda(x) = \Lambda_0 F(x)$ and introducing the potential $\mathbf{J} = \mathrm{rot}(\Psi_X\hat{\mathbf{z}}) = (2\phi_0/\mu_0\Lambda_0)\mathrm{rot}(\psi_X\hat{\mathbf{z}})$, we get

$$\Big[-F(x)\nabla^2 - F'(x)\frac{\partial}{\partial x}\Big]\psi_X(x,y) = \delta^{(2)}(\mathbf{r}-\mathbf{r_v}). \tag{23}$$

It is worth noting that when $F = 1$, we have a uniform Λ, which reproduces Eq. (4). The Fourier transform of Eq. (23) is

$$\Big(-F\frac{\partial^2}{\partial x^2} + k^2 F - F'\frac{\partial}{\partial x}\Big)\tilde{\psi}_X(x,k) = \delta(x-X). \tag{24}$$

We obtain the solution of Eqs. (23) or (24) below.

We begin by considering a special case where $F(x)$ is slowly varying. When the typical length scale of the spatial variation of F is much larger than that of ψ, we can approximate F as quasihomogeneous. Under this assumption, Eq. (24) reduces to the quasihomogeneous equation, $F(x)(-\partial_x^2 + k^2)\psi_X^{\mathrm{qh}} = \delta(x-X)$. The solution is $\tilde{\psi}_X^{\mathrm{qh}}(x,k) = \tilde{\psi}_X^{\mathrm{hmg}}(x,k)/F(X)$. Here, $\tilde{\psi}_X^{\mathrm{hmg}}$ is the solution for the homogeneous film ($F = 1$) and is given by Eq. (9). This assumption holds true in the proximity of the vortex core, hence allowing us to derive

$$\tilde{\psi}_X(X_\xi,k) \to \tilde{\psi}_X^{\mathrm{qh}}(X_\xi,k) \quad (\text{for } kW \gg 1), \tag{25}$$

$$\tilde{\psi}_X^{\mathrm{qh}}(X_\xi,k) = \frac{\cosh k(W-\xi) - \cosh 2kX}{2kF(X)\sinh kW}. \tag{26}$$

This observation will be useful in the computation of the vortex self-energy in the following.

The self energy ϵ can be calculated from the formula given by Eq. (12). Although this formula was derived for a superconducting thin film with uniform λ, it can also be applied to the case where λ is nonuniform, as shown in Appendix A. Our task is to integrate $\tilde{\psi}_X(X_\xi,k)$ over the k space, and to facilitate convergence of the integral, we employ a trick. Specifically, we split the integrand into two parts: $\tilde{\psi}_X(X_\xi,k) = [\tilde{\psi}_X(X_\xi,k) - \tilde{\psi}_X^{\mathrm{qh}}(X_\xi,k)] + $

$\tilde{\psi}_X^{\mathrm{qh}}(X_\xi,k)$. This yields

$$\frac{\epsilon(X)}{\epsilon_0} = L_0(X) + L_1(X), \tag{27}$$

$$L_0 = \int_{-\infty}^{\infty} dk\tilde{\psi}_X^{\mathrm{qh}}(X_\xi,k) = \frac{1}{F(X)}\ln\Big[\frac{2W}{\pi\xi}\cos\frac{\pi X}{W}\Big], \tag{28}$$

$$L_1 = \int_{-\infty}^{\infty} dk\Big[\tilde{\psi}_X(X_\xi,k) - \tilde{\psi}_X^{\mathrm{qh}}(X_\xi,k)\Big]. \tag{29}$$

In Sec. II A, we obtained an analytical expression for the integral of L_0 by evaluating it explicitly. In contrast, the integral of L_1 needs to be computed numerically, but it converges rapidly thanks to Eq. (25). To perform this numerical evaluation, we introduce a cutoff k_c. For instance, setting $k_cW \sim 30$–40 is sufficient to obtain an accuracy of $\lesssim 1\%$ across a broad range of parameter values used in the subsequent subsections. Furthermore, when a vortex approaches the edge, the length scale of the spatial variation of $\tilde{\psi}$ decreases due to the boundary condition, making the quasi-homogeneous contribution L_0 dominant. This leads to the following equation.

$$\frac{\epsilon(X)}{\epsilon_0}\Big|_{X\simeq\pm W/2} \simeq L_0(X) = \frac{1}{F(X)}\ln\Big[\frac{2W}{\pi\xi}\cos\frac{\pi X}{W}\Big]. \tag{30}$$

The magnetic potential $U = -\mu_z B$ also contributes to the free energy. The magnetic moment μ_z can be obtained from Eq.(15) using $\tilde{\psi}(x,0)$, which is the solution of Eq. (24) for $k = 0$. Therefore, we arrive at

$$\mu_z(X) = \frac{2\phi_0}{\mu_0\Lambda_0}\int_{-W/2}^{W/2} dx\tilde{\psi}_X(x,0), \tag{31}$$

$$\Big(-F\frac{\partial^2}{\partial x^2} - F'\frac{\partial}{\partial x}\Big)\tilde{\psi}_X(x,0) = \delta(x-X). \tag{32}$$

The free energy $G = \epsilon - \mu_z B$ reduces to

$$\frac{G(X)}{\epsilon_0} = \frac{\epsilon(X)}{\epsilon_0} - \frac{B}{B_\phi}\frac{8}{W^2}\int_{-W/2}^{W/2} dx\tilde{\psi}_X(x,0) \tag{33}$$

The critical field B_{c1} can be calculated from the condition $G(0) = 0$ or

$$B_{c1} = \frac{\epsilon(0)}{\mu_z(0)} = \frac{B_\phi\int_{-\infty}^{\infty} dk\tilde{\psi}_{X=0}(0,k)}{(8/W^2)\int_{-W/2}^{W/2} dx\tilde{\psi}_{X=0}(x,0)}. \tag{34}$$

In order to calculate $G(X)$ and B_{c1}, a specific Pearl length distribution is required. We address it in the next subsection.

As an example of how to implement an inhomogeneous $\Lambda(x)$ into a film, let us consider doping impurities. In the

dirty limit, we know that $\lambda \propto \sqrt{\Gamma_{\text{imp}}}$, where Γ_{imp} is the impurity scattering rate, so we have $\Lambda(x) \propto \Gamma_{\text{imp}}(x)$. Thus, the impurity profile corresponds to the target $\Lambda(x)$ profile, making this one way to implement it.

Note that impurity doping can affect the coherence length, which is given by $\xi(x) \propto 1/\sqrt{\Gamma_{\text{imp}}(x)} \propto 1/\sqrt{F(x)}$. This variation in $\xi(x)$ appears in the standard cutoff of the logarithmic divergence, $\ln(W/\xi)$, which is used in the evaluation of the vortex self-energy in the London theory [see Eqs. (14) and (27)]. However, it is well known that this artificial cutoff is a qualitative prescription to evaluate vortex self-energy in the London theory, and we should not take seriously a small variation of ξ. Moreover, even if we take a variation of ξ into account, its impact on $\ln(W/\xi)$ is usually negligible. Therefore, in this section, we assume that ξ is constant and independent of $\Lambda(x)$.

See also Appendix B for a specific method suggestion on controlling the inhomogeneity of Pearl length through doping impurities.

2. Example: quadratic $\Lambda(x)$

In principle, we could consider any distribution of $\Lambda(x)$ in our analysis. However, for the purpose of illustrating the method of edge-barrier engineering, it is useful to consider a simple model that captures its essence. We thus adopt a quadratic distribution given by

$$\Lambda(x) = \Lambda_0 F(x), \tag{35}$$

$$F(x) = \gamma\left(\frac{x^2}{W^2} - \frac{1}{4}\right) + 1. \tag{36}$$

Here, Λ_0 represents the Pearl length at the edges of the film, and the parameter γ controls the variation of Λ in the region $-W/2 < x < W/2$. Specifically, for $\gamma < 0$ and $\gamma > 0$, $\Lambda(0) > \Lambda_0$ and $\Lambda(0) < \Lambda_0$, respectively. It is worth noting that $\gamma = -\infty$ and $\gamma = 4$ correspond to $\Lambda(0) = \infty$ and $\Lambda(0) = 0$, respectively. A homogeneous film is
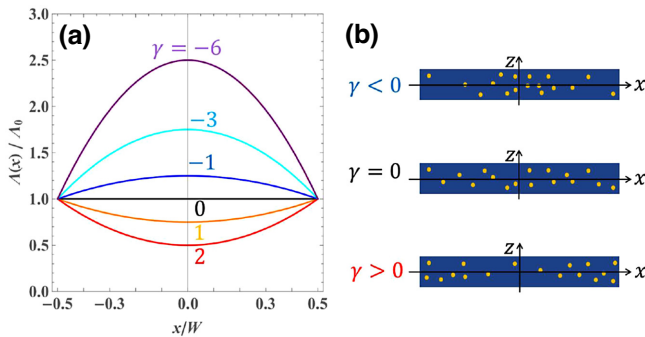
FIG. 3. (a) Inhomogeneous distribution of Λ given by Eqs. (35) and (36). (b) Inhomogeneous impurity distributions as examples of methods to implement inhomogeneous Λ distributions.
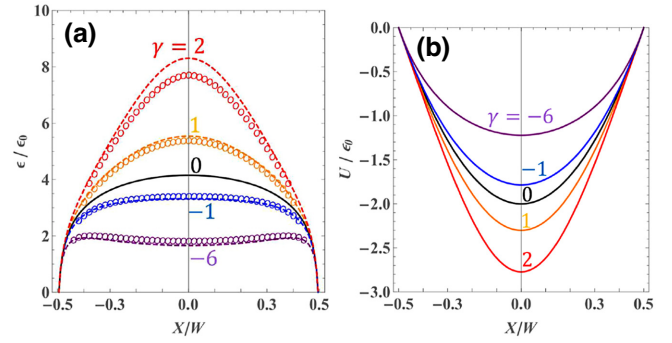
FIG. 4. (a) Influence of inhomogeneous Λ on the vortex self-energy ϵ. The circles represent numerically calculated ϵ for an inhomogeneous film using Eq. (27), while the dashed curves are calculated based on Eq. (30). The black curve corresponds to the homogeneous film. (b) Impact of inhomogeneous Λ on $U = -\mu_z B$ calculated using Eq. (39). All calculations in the figures are performed with $\xi/W = 0.01$.

obtained when $\gamma = 0$. Figure 3 shows the Pearl-length distribution $\Lambda(x)$ for different values of γ.

Using the formulation developed in Sec. II B 1, we can calculate the self-energy from Eq. (27). As shown in Fig. 4(a), the self-energy of a vortex located at $x = X$ varies depending on the value of γ. When $\gamma > 0$, the self-energy of a vortex is larger than that of the homogeneous case ($\gamma = 0$), particularly in the middle of the strip due to the shorter Pearl length. On the other hand, when $\gamma < 0$, the self-energy of a vortex is smaller than that of the homogeneous case. It is worth noting that the dashed curves, obtained from Eq. (30), accurately represent the behavior near the edges of the strip. However, it is interesting to observe that this equation also provides a reasonably good approximation in the middle of the strip, covering a wide range of inhomogeneity parameters.

To obtain the magnetic moment, we can use Eqs. (31) and (32). Here, $\tilde{\psi}_X(x, 0)$ is given by

$$\tilde{\psi}_X(x, 0) = C_\pm\left(\tan^{-1}\frac{\sqrt{\gamma}}{\sqrt{4 - \gamma}} \mp \tan^{-1}\frac{2x\sqrt{\gamma}}{W\sqrt{4 - \gamma}}\right), \tag{37}$$

$$C_\pm = W\frac{\tan^{-1}\frac{\sqrt{\gamma}}{\sqrt{4-\gamma}} \pm \tan^{-1}\frac{2X\sqrt{\gamma}}{W\sqrt{4-\gamma}}}{\sqrt{(4 - \gamma)\gamma}\,\tan^{-1}\frac{\sqrt{\gamma}}{\sqrt{4-\gamma}}} \tag{38}$$

for $x \geq X$ and $x \leq X$, respectively. A similar calculation for a film containing an antivortex introduces an additional factor of (-1). Then, the magnetic moment can be computed as

$$\mu_z(X) = \pm\frac{\phi_0 W^2}{\mu_0 \Lambda_0 \gamma}\ln\frac{4}{4 - \gamma + 4\gamma(X/W)^2}, \tag{39}$$

for a film including a vortex and an antivortex, respectively. Notably, when γ approaches 0, Eq. (39) reduces to the magnetic moment of the homogeneous case given by Eq. (16). Figure 4(b) shows the magnetic potential $U = -\mu_z B$ for a film including a vortex (antivortex) in the magnetic field $B = +2B_\phi$ ($B = -2B_\phi$). For $\gamma > 0$, U is more stable than in the homogeneous case.

Figure 5 illustrates the impact of an inhomogeneous $\Lambda(x)$ on the free energy $G = \epsilon - \mu_z B$ of a film containing a vortex in a magnetic field $B \geq 0$. The effect of inhomogeneity on ϵ is dominant compared to U, as demonstrated in Fig. 4, and a positive (negative) γ destabilizes (stabilizes) the vortex state. Notably, when $\gamma = -6$ [Fig. 5(a)], the inhomogeneity stabilizes the vortex state, and the free

energy features a metastable minimum even at $B = 0$. As γ increases, the vortex state is destabilized [e.g., compare the black curves in Figs. 5(a)–5(d)]. This results in an increase in the critical field B_{c1}. Figure 5(e) shows B_{c1} as a function of the inhomogeneity parameter γ calculated from Eq. (34), indicating that an inhomogeneous $\Lambda(x)$ can be employed to engineer B_{c1}.

Previously, it was thought that the critical field B_{c1} of a narrow thin-film strip is almost independent of material parameters, and the only practical way to increase B_{c1} was to decrease the strip width. However, we have now discovered that this constraint applies only to homogeneous materials, and we have found another way to increase B_{c1}: by designing an inhomogeneous $\Lambda(x)$.

III. CRITICAL CURRENT

The method of engineering the free-energy profile is applicable to systems regardless of the presence or absence of a bias current. This naturally leads to the question: what is the impact of an inhomogeneous Pearl length on the critical current? In this section, we will delve into this topic and investigate it further.

A. Critical current in a *homogeneous* narrow thin-film strip

To begin, we will provide a brief overview of the critical current in a homogeneous narrow thin-film strip. Consider a bias current I flowing along the longitudinal direction. The sheet bias-current density is given by $J_b = I/W$. Then, the free energy of a system containing a vortex or an antivortex located at $\mathbf{r}_v = (X, 0)$ can be expressed as follows:

$$G(X) = \epsilon(X) - \mu_z(X)B + \Delta G(X). \qquad (40)$$

Here, the vortex self-energy $\epsilon(X)$ and the film's magnetic moment $\mu_z(X)$ in a homogeneous film are given by Eqs. (14) and (16), respectively. The final term $\Delta G(X)$ represents the work done by the Lorentz force and is expressed as

$$\Delta G(X) = \mp I\phi_0 \left[\frac{X}{W} \pm \frac{\mathrm{sgn}(I)}{2} \right] \qquad (41)$$

for a vortex and an antivortex, respectively, where sgn is the sign function of the current I, i.e., $\mathrm{sgn}(I) = \pm 1$ for $I = \pm|I|$, respectively (see Fig. 6). Therefore, we obtain [47,62,66]

$$\frac{G(X)}{\epsilon_0} = \ln\left(\frac{2W}{\pi\xi} \cos\frac{\pi X}{W} \right) \mp \frac{B}{B_\phi}\left(1 - 4\frac{X^2}{W^2} \right)$$
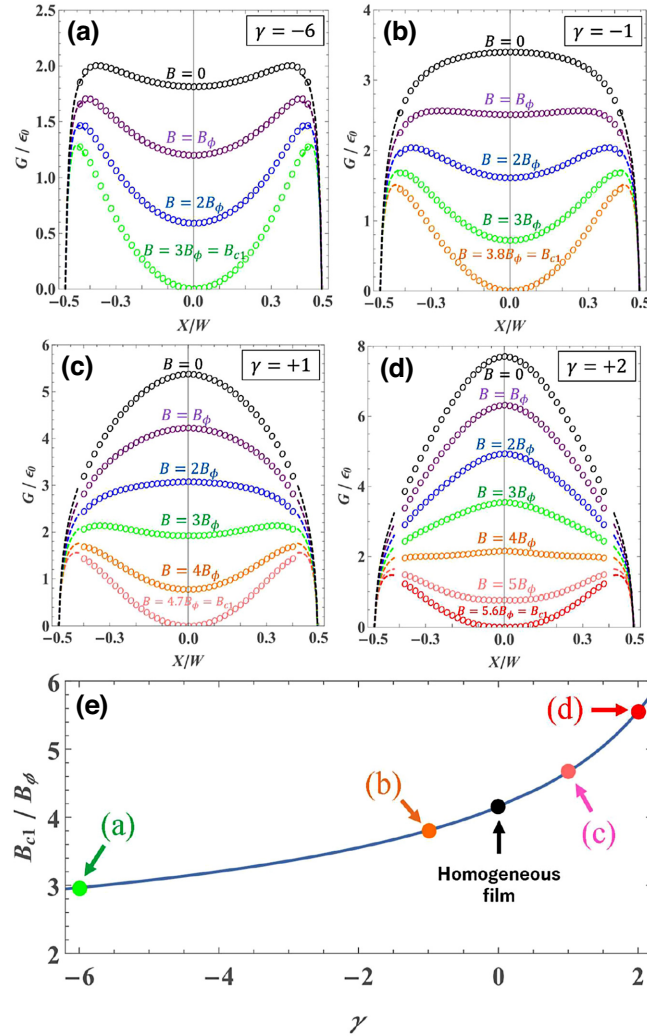$$\mp \frac{I}{I_0}\left[\frac{X}{W} \pm \frac{\mathrm{sgn}(I)}{2} \right]. \qquad (42)$$

FIG. 5. (a)–(d) Influence of an inhomogeneous $\Lambda(x)$ on the free energy $G = \epsilon - \mu_z B$ in a system with a vortex located at $x = X$. The $\Lambda(x)$ distribution is defined by Eqs. (35) and (36) [see also Fig. 3(a)]. The dashed curves near the edges are calculated using Eq. (30). (e) Variation of the critical field B_{c1} as a function of the inhomogeneity parameter γ. The coherence length is fixed at $\xi/W = 0.01$ for all calculations in the figures.
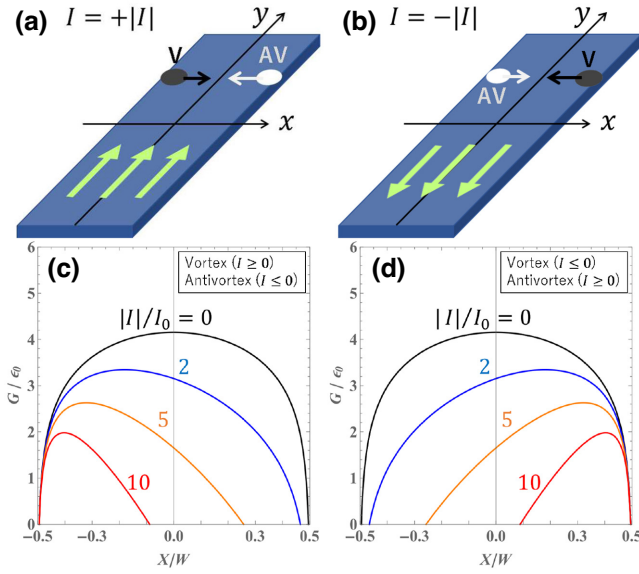
FIG. 6. (a),(b) Schematic illustrations of the Lorentz forces acting on a vortex and an antivortex in a narrow thin-film strip. (c),(d) Impact of the bias current on the free energy of a homogeneous narrow thin-film strip containing a vortex and an antivortex at $x = X$, with $B = 0$.

Here, I_0 is introduced as

$$I_0 = \frac{\phi_0}{2\pi\mu_0\Lambda}. \tag{43}$$

To understand the typical magnitude of I_0, we can write $I_0 = (\xi/W)(\phi_0/4\pi\mu_0\lambda^2\xi)(Wd)$. Since the second factor is of the order of the depairing current density and the third factor is the cross-section area of the strip, we find that I_0 is smaller than the depairing current I_d by a factor of ξ/W.

The vortex-entry current I_V (or antivortex-entry current I_{AV}) corresponds to the current at which the edge barrier disappears. The condition of the disappearance of the edge barrier can be expressed as

$$G(X_p; I_{V,AV}, B) = 0, \tag{44}$$

where X_p is the peak position of the edge barrier and satisfies $G'(X_p; I_{V,AV}, B) = 0$. Solving Eq. (44), we obtain [47,62,66,69] (see also Appendix C)

$$I_V^{(\pm)} = I_0\left(\frac{2W}{e\xi} - 4\frac{B}{B_\phi}\right), \tag{45}$$

$$I_{AV}^{(\pm)} = I_0\left(\frac{2W}{e\xi} + 4\frac{B}{B_\phi}\right). \tag{46}$$

The superscript $(\pm)$ indicates the direction of the current, but both I_V and I_{AV} are independent of the current direction. Here, $e = 2.718$ is Napier's constant. The critical current is given by

$$I_c^{(\pm)} = \min\{I_V^{(\pm)}, I_{AV}^{(\pm)}\} = \begin{cases} I_V^{(\pm)} & (B \geq 0) \\ I_{AV}^{(\pm)} & (B \leq 0) \end{cases}. \tag{47}$$

Note that $I_c \sim (W/\xi)I_0$, indicating that the magnitude of I_c is approximately equal to the depairing current, $I_c \sim I_d$. Additionally, I_c is direction independent. For applied currents greater than I_c, the motion of vortices across the film from one edge to another becomes unavoidable, leading to the appearance of a finite resistance.

The linear dependence of I_c on the magnetic field B holds for relatively small values of B. When the magnetic field reaches a critical value B_{stop}, a free energy minimum appears at a point X_s where $G'(X_s; I_c, B_{stop}) = 0$, and penetrating vortices start to reside in the minimum [66,67]. As these vortices carry a current, they begin to affect the barrier and modify the behavior of I_c. The critical value B_{stop} can be calculated by considering the condition for the existence of a solution X_s that satisfies $G'(X_s; I_c, B_{stop}) = 0$. For a homogeneous film, we obtain

$$B_{stop} = \left(s + \frac{1}{4} + \frac{1}{4}\sqrt{8s + 1}\right)B_\phi. \tag{48}$$

Here, $s = W/4e\xi$. When $\xi/W \ll 1$, Eq. (48) reduces to $B_{stop} \sim sB_\phi = \phi_0/2\pi eW\xi$ [66,67]. For example, if $\xi/W = 0.005$, we have $s = 18$ and $B_{stop} \simeq 22B_\phi$.

B. Critical current in an *inhomogeneous* narrow thin-film strip

1. Formulation

Let us develop the formulation for the critical current in an inhomogeneous narrow thin-film strip. When we consider a system with a vortex or an antivortex located at position $\mathbf{r}_v = (X, 0)$ in a film with an inhomogeneous $\Lambda(x)$, the free energy of the system is given by Eq. (40). In an inhomogeneous film, the vortex self-energy $\epsilon(X)$ and the film's magnetic moment $\mu_z(X)$ are given by Eq. (27) and Eqs. (31) and (32), respectively. The last term $\Delta G(X)$ corresponds to the work done by the Lorentz force coming from a finite bias current. It is worthwhile to note that the sheet bias current density J_b is no longer uniform and proportional to the local superfluid density $\Lambda^{-1}(x)$. Rather, it is given by

$$J_b(x) = \frac{I/\Lambda(x)}{\int_{-W/2}^{W/2} dx[1/\Lambda(x)]} = \frac{I/F(x)}{\int_{-W/2}^{W/2} dx[1/F(x)]}. \tag{49}$$

It is easy to check that when $\Lambda(x)$ is uniform ($F = 1$), the sheet bias current density J_b is also uniform and given by

$J_b = I/W$. Then, we obtain (see also Fig. 6)

$$\Delta G(X) = \mp I\phi_0 \frac{\int_{\mp x_e}^X [1/F(x)]}{\int_{-W/2}^{W/2} dx[1/F(x)]}, \qquad (50)$$

for a vortex and an antivortex entry, respectively. Here, $x_e = (W/2)\mathrm{sgn}(I)$.

To calculate the critical current, it is necessary to understand the behavior of $G(X) = \epsilon(X) - \mu_z(X)B + \Delta G(X)$ near the edges of the film. Fortunately, in this case, Eq. (30) provides an analytical expression for $\epsilon(X)$. It should be noted that the coherence length ξ depends on x, but we need only its value at the edge where the edge barrier disappears. For certain functions $F(x)$, we can derive analytical expressions for both $\mu_z(X)$ and $\Delta G(X)$, allowing us to obtain an analytical expression for the critical current I_c. Examples of these expressions will be presented in the following subsections.

2. Example: quadratic $\Lambda(x)$

Let us examine the impact of an inhomogeneous distribution of $\Lambda(x)$ on the critical current, considering the same distribution as in Sec. II B 2 [described by Eqs. (35) and (36) and shown in Fig. 3]. Starting from the expression $G(X) = \epsilon(X) - \mu_z(X)B + \Delta G(X)$, we can utilize the self-energy expression given by Eq. (27) and the magnetic moment μ_z derived in Sec. II B 2 [given by Eq. (39)]. The third term is influenced by the sheet bias-current distribution $J_b(x)$, which is determined by the inhomogeneous $\Lambda(x)$. Figure 7(a) illustrates $J_b(x)$ for different values of γ calculated using Eq. (49). Here, $J_{b,\mathrm{hmg}} = I/W$. For $\gamma > 0$ ($\gamma < 0$), the superfluid density is higher (lower) in the middle. Consequently, the current is more pronounced in the middle (reduced at the edges), leading to a suppression (enhancement) of the current at the edges. Then, Eq. (50) yields

$$\Delta G(X) = \mp \frac{I}{2I_0}\left(\frac{\tan^{-1}\frac{2X}{W}\sqrt{\frac{\gamma}{4-\gamma}}}{\tan^{-1}\sqrt{\frac{\gamma}{4-\gamma}}} \pm \mathrm{sgn}(I)\right), \qquad (51)$$

for a vortex and an antivortex entry, respectively. Here, $I_0 = \phi_0/2\pi\mu_0\Lambda_0$. Combining these expressions, we obtain

$$\frac{G(X)}{\epsilon_0} = \frac{\epsilon(X)}{\epsilon_0} \mp \frac{B}{B_\phi}\frac{4}{\gamma}\ln\frac{4}{4-\gamma+4\gamma(X/W)^2}$$

$$\mp \frac{I}{2I_0}\left(\frac{\tan^{-1}\frac{2X}{W}\sqrt{\frac{\gamma}{4-\gamma}}}{\tan^{-1}\sqrt{\frac{\gamma}{4-\gamma}}} \pm \mathrm{sgn}(I)\right), \qquad (52)$$

for a vortex and an antivortex entry, respectively. In the vicinity of the film edges, the self-energy $\epsilon(X)$ can be analytically expressed using Eq. (30). This analytical
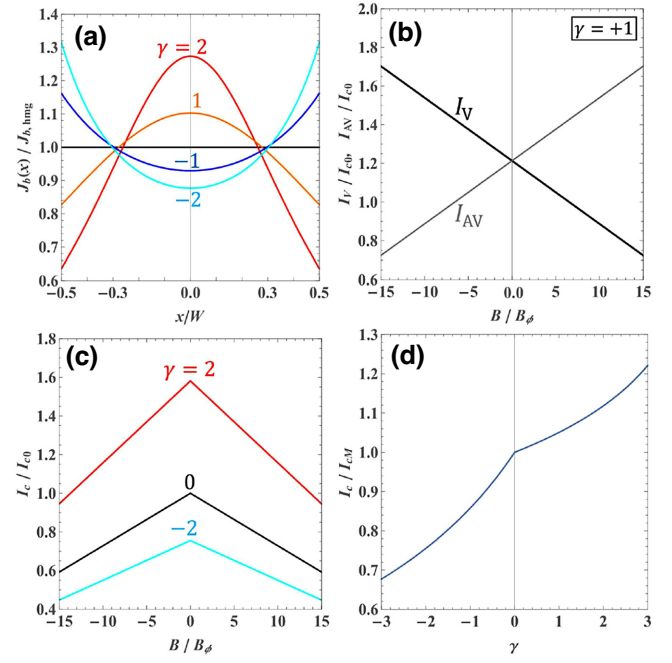

FIG. 7. (a) Influence of the inhomogeneity parameter γ on the sheet bias-current density $J_b(x)$. Here, $J_{b,\mathrm{hmg}} = I/W$ [see also Fig. 3(a)]. (b) Vortex-entry current I_V and antivortex-entry current I_{AV} as a function of the external magnetic field B. Here, $I_{c0} = (2W/e\xi_e)I_0 = \phi_0 W/e\pi\mu_0\xi_e\Lambda_0$, where e is Napier's constant and $\xi_e = \xi(\pm W/2)$ is the coherence length at the edges. (c) Critical currents $I_c = \min\{I_V, I_{AV}\}$ for $\gamma = 2, 0, -2$ as a function of B. (d) Comparison of I_c between an inhomogeneous film with $\Lambda(x)$ and a homogeneous film with the shortest Pearl length $\Lambda_{\mathrm{hmg}} = \Lambda_0\min F(x)$. Here, $I_{cM} = \phi_0 W/e\pi\mu_0\xi_{\mathrm{hmg}}\Lambda_{\mathrm{hmg}}$. For all calculations in the figures, we have assumed $\xi_e/W = 0.005$ at the edges.

expression is sufficient for the calculation of the critical current I_c.

The calculations of the vortex-entry current and the antivortex-entry current can be performed straightforwardly using Eqs. (30) and (52) and the condition of the disappearance of the edge barrier given by Eq. (44). We get (see Appendix C)

$$I_V^{(\pm)} = \frac{4I_0\tan^{-1}\sqrt{\frac{\gamma}{4-\gamma}}}{\sqrt{\gamma(4-\gamma)}}\left(\frac{2W}{e\xi_e} - \frac{4B}{B_\phi}\right), \qquad (53)$$

$$I_{AV}^{(\pm)} = \frac{4I_0\tan^{-1}\sqrt{\frac{\gamma}{4-\gamma}}}{\sqrt{\gamma(4-\gamma)}}\left(\frac{2W}{e\xi_e} + \frac{4B}{B_\phi}\right). \qquad (54)$$

Here, $\xi_e = \xi(\pm W/2)$. It is worthwhile to note that when performing these calculations, the coherence length at the edges should be used as an input parameter. Figure 7(b) illustrates the values of $I_V = I_V^{(\pm)}$ and $I_{AV} = I_{AV}^{(\pm)}$ for $\gamma = 1$. Due to the system's symmetry, we have $I_V = I_{AV}$ at $B = 0$ (see also Fig. 6). For $B > 0$ ($B < 0$), the vortex

state (antivortex state) is stabilized, resulting in $I_V < I_{AV}$ ($I_{AV} < I_V$).

The critical current can be determined using the expression $I_c = I_c^{(\pm)} = \min\{I_V^{(\pm)}, I_{AV}^{(\pm)}\}$. Figure 7(c) illustrates the variation of the critical current I_c for different values of γ. It should be noted that, as discussed in Sec. III A, the linear dependence of I_c on B ceases to hold when $B \geq B_{\text{stop}}$. In an inhomogeneous film, B_{stop} is no longer given by Eq. (48) and depends on the inhomogeneity parameter γ. However, as shown in Appendix D, we typically have $B_{\text{stop}}(\gamma) \gtrsim 20$ for $\gamma \gtrsim -3$. Within the range of the plotted data, the linearity of the critical current with respect to B continues to hold.

Now, let us investigate whether an inhomogeneous film can enhance the critical current. We assume that the inhomogeneity arises from a nonuniform impurity concentration. In a homogeneous film with a constant value of Λ_{hmg}, the critical current is given by the formula $I_c = \phi_0 W / e \pi \mu_0 \xi_{\text{hmg}} \Lambda_{\text{hmg}}$ at $B = 0$. Unlike the critical field B_{c1}, the critical current of a homogeneous film can be improved by simply reducing the product $\xi_{\text{hmg}} \Lambda_{\text{hmg}}$. This suggests that instead of creating an inhomogeneous film with varying $\Lambda(x)$, we can achieve an increase in the critical current by using a homogeneous film with a lower impurity concentration. Assuming the capability to fabricate an inhomogeneous film with varying $\Lambda(x)$, it is also assumed that we have the technology to create a corresponding homogeneous film with $\Lambda_{\text{hmg}} = \min \Lambda(x) = \Lambda_0 \min F(x)$. Here, $\min F(x) = 1$ for $\gamma \leq 0$ and $\min F(x) = F(0) = 1 - \gamma/4$ for $\gamma \geq 0$ (see Fig. 3). The coherence length of such a homogeneous film is given by $\xi_{\text{hmg}} = \xi_e / \sqrt{\min F(x)}$. In this context, we are interested in comparing the critical current I_c of the inhomogeneous film with varying $\Lambda(x)$ to the critical current I_{cM} of the homogeneous film with a constant Λ_{hmg}. Figure 7(d) illustrates this comparison, clearly demonstrating that an inhomogeneous film with $\gamma > 0$ (lower impurity concentration in the middle of the strip) consistently exhibits a larger critical current compared to the homogeneous film. The enhancement in critical current is attributed to the current-suppression effect at the edges [see Fig. 7(a)]. This mechanism is analogous to the superheating field enhancement structure studied in superconducting resonator technology for particle accelerators [30–36]. These results indicate that, for the purpose of enhancing the critical current, utilizing an inhomogeneous film with an optimally designed $\Lambda(x)$ is preferable over a homogeneous film.

3. Example: left-right asymmetric linear $\Lambda(x)$ and superconducting diode effect

As we saw in Sec. III A, the critical current of a homogeneous film does not depend on the direction of the current. This remains true even for an inhomogeneous film with the quadratic $\Lambda(x)$ given by Eqs. (35) and (36), as discussed

in Sec. III B 2. This fact is summarized by the vanishing of the superconducting diode quality parameter η, which measures the nonreciprocity of the critical current,

$$\eta = \frac{I_c^+ - I_c^-}{I_c^+ + I_c^-}. \tag{55}$$

It is known that η is nonzero only when inversion and time-reversal symmetries are broken.

To induce a nonzero η in our system, a combination of the unequal disappearance of the vortex energy barrier at the edges and an external magnetic field is required. This can be qualitatively understood through the following discussion: suppose we assume that the left edge is weaker than the right edge. In the absence of an external magnetic field ($B = 0$), a vortex enters the film from the left edge for $I > 0$, while an antivortex enters from the left edge for $I < 0$ [see Figs. 6(a) and 6(b)]. Despite the sign of I changing the type of penetration (vortex or antivortex), the critical current (I_c) remains unaffected since it is determined by the properties of the left edge: $I_c^{(+)} = I_c^{(-)}$. However, when an external magnetic field is applied ($B > 0$ or $B < 0$), the vortex (or antivortex) state becomes preferred, resulting in $I_c^{(+)} < I_c^{(-)}$ (or $I_c^{(+)} > I_c^{(-)}$), thus showcasing the nonreciprocity of the critical current. Therefore, the combination of the unequal disappearance of the vortex energy barrier at the edges and the external magnetic field, which causes the vortex-antivortex asymmetry, is necessary to induce the nonreciprocity.

While any form of $\Lambda(x)$ can be used as long as it is left-right asymmetric, we consider the following simplest form in this paper [see Fig. 8(a)]:

$$\Lambda(x) = \Lambda_0 F(x), \tag{56}$$

$$F(x) = 2\alpha \frac{x}{W} + 1. \tag{57}$$

Here, $\Lambda_0 = [\Lambda(W/2) + \Lambda(-W/2)]/2$, $\alpha = [\Lambda(W/2) - \Lambda(-W/2)]/[\Lambda(W/2) + \Lambda(-W/2)]$. For instance, $\alpha = 0.5$ corresponds to $\Lambda(W/2)/\Lambda(-W/2) = 3$. The inhomogeneous $\Lambda(x)$ distribution leads to a nonuniform sheet bias-current density J_b, which can be obtained using Eq. (49). Figure 8(b) displays the profiles of $J_b(x)$ for different values of α.

Let us analyze the free energy $G = \epsilon - \mu_z B + \Delta G$. The magnetic potential term is computed using Eqs. (31) and (32). The solution of Eq. (32) is given by

$$\tilde{\psi}_X(x, 0) = \frac{-W}{4\alpha \tanh^{-1} \alpha} \ln \frac{1 \mp \alpha}{1 + 2\alpha \frac{X}{W}} \ln \frac{1 \pm \alpha}{1 + 2\alpha \frac{x}{W}} \tag{58}$$

for $x \geq X$ and $x \leq X$, respectively. A similar calculation for a film containing an antivortex introduces an additional factor of (-1). Using Eq. (31), we get the magnetic
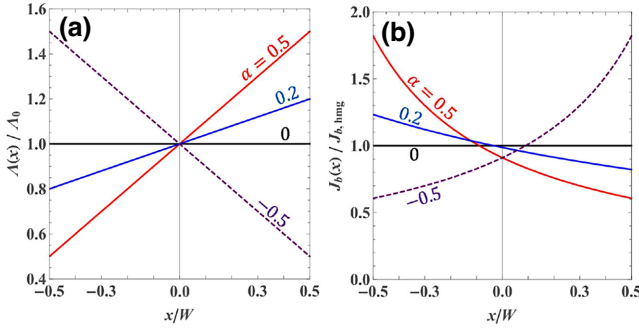
FIG. 8. (a) Examples of left-right asymmetric Pearl-length distribution $\Lambda(x)$ given by Eqs. (56) and (57) for different α values. (b) Sheet bias-current distributions $J_b(x)$ for different α values. Here, $J_{\mathrm{hmg}} = I/W$ is the sheet bias-current for a homogeneous strip.

moment

$$
\mu_z(X) = \frac{\pm\phi_0 W^2}{2\mu_0 \Lambda_0 \alpha \tanh^{-1}\alpha}\left[-\ln\sqrt{1-\alpha^2} - \frac{X}{W}\ln\frac{1+\alpha}{1-\alpha}\right.
$$
$$
\left. + \ln\left(1+2\alpha\frac{X}{W}\right)\right] \tag{59}
$$

for a film containing a vortex and antivortex, respectively. The work done by the Lorentz force can be calculated from Eq. (50), and we get

$$
\Delta G(X) = \mp I\phi_0 \frac{\ln[(1+2\alpha X/W)/\{1\mp\alpha\,\mathrm{sgn}(I)\}]}{\ln[(1+\alpha)/(1-\alpha)]}. \tag{60}
$$

Combining these terms, we obtain

$$
\frac{G(X)}{\epsilon_0} = \frac{\epsilon(X)}{\epsilon_0} \mp \frac{B}{B_\phi}\frac{2}{\alpha\tanh^{-1}\alpha}\left[-\ln\sqrt{1-\alpha^2}\right.
$$
$$
\left. - \frac{X}{W}\ln\frac{1+\alpha}{1-\alpha} + \ln\left(1+2\alpha\frac{X}{W}\right)\right]
$$
$$
\mp \frac{I}{I_0}\frac{\ln[(1+2\alpha X/W)/\{1\mp\alpha\,\mathrm{sgn}(I)\}]}{\ln[(1+\alpha)/(1-\alpha)]} \tag{61}
$$

for a vortex and antivortex, respectively. The vortex self-energy term $\epsilon(X)$ is calculated using Eq. (27) for the region $-W/2 < X < W/2$, while the analytical expression provided by Eq. (30) is applicable for the edges.

The vortex-entry current $I_V^{(\pm)}$ and the antivortex-entry current $I_{AV}^{(\pm)}$ can be determined by calculating the current at which the edge barrier disappears, as discussed in Secs. III A and III B 2, using Eq. (44). We find (see Appendix C)

$$
\frac{I_V^{(\pm)}}{I_0} = \frac{\ln[(1+\alpha)/(1-\alpha)]}{2\alpha}\left[\frac{2W}{e\xi_{L,R}} \mp \frac{2(B/B_\phi)}{\alpha\tanh^{-1}\alpha}\right.
$$
$$
\left. \times\left\{2\alpha - (1\mp\alpha)\ln\frac{1+\alpha}{1-\alpha}\right\}\right], \tag{62}
$$

$$
\frac{I_{AV}^{(\pm)}}{I_0} = \frac{\ln[(1+\alpha)/(1-\alpha)]}{2\alpha}\left[\frac{2W}{e\xi_{R,L}} \mp \frac{2(B/B_\phi)}{\alpha\tanh^{-1}\alpha}\right.
$$
$$
\left. \times\left\{2\alpha - (1\pm\alpha)\ln\frac{1+\alpha}{1-\alpha}\right\}\right]. \tag{63}
$$

Here, $\xi_L = \xi(-W/2)$ and $\xi_R = \xi(+W/2)$. It is useful to note that in the calculations of $I_{V,AV}^{(\pm)}$, the coherence lengths at the edges are required. In this section, we consider the inhomogeneity to be a result of variations in impurity concentration. To determine the coherence length at the edges, we calculate $\xi_L = \xi_M/\sqrt{F(-W/2)} = \xi_M/\sqrt{1-\alpha}$ and $\xi_R = \xi_M/\sqrt{F(W/2)} = \xi_M/\sqrt{1+\alpha}$, where $\xi_M = \xi|_{x=0}$ represents the coherence length at the middle of the strip.

Figure 9(a) presents examples of $I_V^{(+)}$ and $I_{AV}^{(+)}$. At $B = 0$, we find that $I_V^{(+)} < I_{AV}^{(+)}$, which is in contrast to the left-right symmetric cases discussed in the previous subsections where $I_V^{(+)} = I_{AV}^{(+)}$ at $B = 0$. One might expect the left edge to have a higher energy barrier compared to the right edge due to the smaller Λ for $\alpha > 0$, leading to the expectation of $I_V^{(+)} > I_{AV}^{(+)}$. However, the strong Lorentz force induced by the enhanced sheet bias current at the left edge [see Fig. 8(b)], resulting from the left-right asymmetric $\Lambda(x)$ distribution, overcomes the barrier and pushes the vortex into the interior of the film. Consequently, for $\alpha > 0$
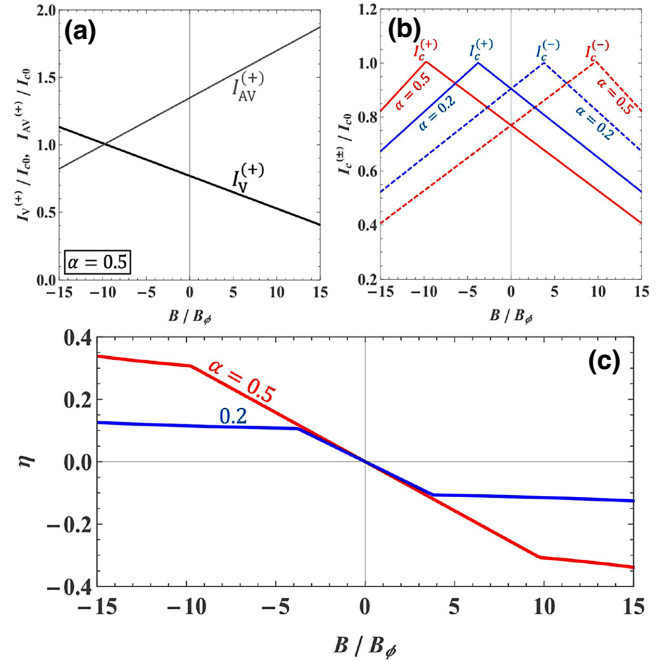

FIG. 9. (a) Examples of $I_V^{(+)}$ and $I_{AV}^{(+)}$, normalized by $I_{c0} = (2W/e\xi)I_0 = \phi_0 W/e\pi\mu_0\xi_M\Lambda_0$. Here, $\xi_M = \xi|_{x=0}$. (b) The critical currents $I_c^{(+)}$ (solid line) and $I_c^{(-)}$ (dashed line) as functions of the external field B for inhomogeneity parameters $\alpha = 0.5$ (red) and 0.2 (blue). (c) The superconducting diode quality parameter η as functions of B for different α. For all calculations in the figures, we have used $\xi_M/W = 0.005$.

at $B = 0$, we observe $I_V^{(+)} < I_{AV}^{(+)}$. As B increases, the vortex state becomes more stable (while the antivortex state becomes less stable), resulting in a decrease in the vortex-entry current I_V and an increase in the antivortex-entry current I_{AV}.

The critical current can be determined straightforwardly by evaluating $I_c^{(\pm)} = \min\{I_V^{(\pm)}, I_{AV}^{(\pm)}\}$. Figure 9(b) shows the critical currents $I_c^{(+)}$ and $I_c^{(-)}$ for various values of α. It can be verified that $I_c^{(+)}$ for $\alpha = 0.5$ is derived from $I_V^{(+)}$ and $I_{AV}^{(+)}$ in Fig. 9(a). The dependence of the maximum values of $I_c^{(\pm)}$ on the inhomogeneity parameter α is found to be remarkably weak. This weak dependence can be attributed to the accidental cancelation between the influences of α and $\xi_{L,R}(\alpha)$ on I_c. Figure 9(c) presents the superconducting diode quality parameter η as a function of B for different values of α. Note that, as demonstrated in Appendix D, the critical value $B_{\text{stop}}(\alpha)$ is greater than 15 for $|\alpha| \lesssim 0.5$. Therefore, within the range of the presented data, the linear relationship between the critical current and magnetic field, B, remains valid.

IV. DISCUSSION

A. Critical field B_{c1} and complete flux expulsion

In Sec. II A, we focused on a homogeneous narrow thin-film strip and reproduced well-established results, such as the free energy G and the critical field B_{c1}. This not only served as a summary of basic knowledge but also familiarized us with our approach in dealing with inhomogeneous systems. As commonly known, the critical field B_{c1} for a homogeneous film is described by Eq. (21), which is nearly independent of material parameters. Consequently, the only viable method to increase B_{c1} was believed to be reducing the film's width W, as discussed in previous studies. However, this constraint is valid solely for homogeneous films, as we demonstrated in Sec. II B.

In Sec. II B, we developed a formulation to calculate the free energy $G = \epsilon - \mu_z B$ of an inhomogeneous film. Specifically, we derived expressions for the self-energy ϵ given by Eqs. (27) and (30). Additionally, the magnetic potential contribution $U = -\mu_z B$ was evaluated using Eq. (31). Employing these formulations, we investigated the effects of a quadratic $\Lambda(x)$ distribution on G and B_{c1} as an illustrative example [see also Fig. 3(a)]. Our findings, depicted in Fig. 5, revealed that inhomogeneities, such as having a shorter Λ in the middle of the strip, can significantly enhance B_{c1}.

One significant application of these findings is the achievement of complete flux expulsion in superconducting films. Previous studies have demonstrated that when the ambient magnetic flux is smaller than the critical field (B_{c1}), it is possible to fully expel the flux from the film. As the critical field increases, the film becomes more resistant to flux trapping. Traditionally, the only method to increase

B_{c1} and promote flux expulsion in homogeneous films was to narrow the strip. However, the introduction of engineered inhomogeneities provides an alternative approach to enhance B_{c1} and make the film robust against flux trapping. This advancement offers greater flexibility in designing superconducting devices with improved flux expulsion capabilities. Furthermore, these findings may offer insights into the flux expulsion phenomenon observed in spatial temperature gradients, which is utilized to enhance the quality factor of particle accelerator cavities [71–75].

In the context of achieving a shorter Pearl length in the middle of the strip with a left-right symmetric nonuniform impurity distribution, a detailed method suggestion is provided in Appendix B.

It is worthwhile to note that even in the absence of vortices and at low microwave frequencies compared to the superconducting gap, a finite surface resistance can arise due to thermally excited quasiparticles [76,77]. This issue is further complicated by various pair-breaking mechanisms originating from the current and resonator materials [27,29,78–86] and the nonequilibrium dynamics of quasiparticles and phonons triggered by subgap and pair-breaking photon [85–91]. Recent research has explored strategies to reduce dissipation by engineering the quasiparticle density of states (DOS), including methods such as applying dc [27,81] or rf [81,85] currents, introducing sparse magnetic impurities [83,85], modifying subgap states through surface processing [6,27,29], or optimizing proximity effects between superconductors and metallic suboxides or hydrides [83,85]. To optimize the quality factor, it is crucial to not only achieve a vortex-free state but also address the engineering of the DOS, as both factors play complementary roles in achieving low dissipation and high-performance superconducting devices.

B. Critical current enhancement and diode effect

In Sec. III B 1, we developed a formulation to evaluate the critical current in an inhomogeneous narrow thin-film strip. In the presence of an inhomogeneous $\Lambda(x)$ distribution, the sheet bias-current density deviates from uniformity and can be described by Eq. (49). Consequently, the contribution of the bias current to the free energy, denoted as ΔG, is given by Eq. (50).

In Sec. III B 2, our focus was specifically on examining the influence of a quadratic $\Lambda(x)$ distribution on the critical current and determining whether the introduction of inhomogeneity could lead to an enhancement in the critical current. Our findings led us to the conclusion that, when the objective is to increase the critical current, it is more advantageous to employ an inhomogeneous film with a reduced Λ value in the middle of the strip, as opposed to a homogeneous film. The enhancement in critical current is attributed to the current suppression effect at the edges induced by the inhomogeneous superfluid density

distribution. This mechanism shares similarities with the superheating field enhancement studied in inhomogeneous structures employed in particle accelerator resonators [30–36]. Future work will involve comparing our findings with microscopic calculations of the depairing current in an inhomogeneous strip. This analysis will provide a more comprehensive understanding of the critical current behavior in such systems.

In Sec. III B 3, we explored the impact of a left-right asymmetric $\Lambda(x)$ distribution, described by Eqs. (56) and (57), on the superconducting diode effect. By deriving the expression for the free energy, Eq. (61), we were able to determine the critical current, as depicted in Fig. 9(b). The critical current depends on the interplay between the left-right asymmetric edge barriers and the left-right asymmetric sheet bias-current distribution. Furthermore, we analyzed the behavior of the superconducting diode quality parameter η with respect to the inhomogeneity parameter α and the external field B, as presented in Fig. 9(c). Our results revealed that increasing the inhomogeneity parameter and the external field led to an enhancement of η, showcasing the potential of engineering inhomogeneous Λ distributions to control and manipulate the superconducting diode effect.

Any left-right asymmetric $\Lambda(x)$ distribution has the potential to induce the superconducting diode effect. In the context of realizing such a distribution through nonuniform impurity doping, we provide a detailed method suggestion in Appendix B. Additionally, an alternative approach involves creating a temperature gradient along the x direction. These methods present innovative avenues for implementing devices that showcase the superconducting diode effect.

APPENDIX A: VORTEX SELF-ENERGY IN AN INHOMOGENEOUS SUPERCONDUCTOR

We extend the method developed by Kogan [63,65] for a homogeneous superconductor to study the behavior of a vortex in an inhomogeneous superconductor. In this case, we consider a superconductor with a nonuniform $\lambda(\mathbf{r})$. The self-energy of a vortex can be divided into two parts.

$$\epsilon = \epsilon_{\text{out}} + \epsilon_{\text{in}}, \tag{A1}$$

$$\epsilon_{\text{out}} = \int dV_{\text{out}} \frac{B^2}{2\mu_0}, \tag{A2}$$

$$\epsilon_{\text{in}} = \int dV_{\text{in}} \left(\frac{B^2}{2\mu_0} + \frac{\mu_0}{2} \lambda^2 j^2 \right). \tag{A3}$$

Here, ϵ_{out} is the magnetic energy outside the material, and ϵ_{in} is the sum of the magnetic energy inside the material and the kinetic energy of the condensate.

Let us start from ϵ_{out}. Since $\text{rot}\mathbf{B} = 0$ in the vacuum, we can introduce a scalar potential φ, which gives $\mathbf{B} = \nabla\varphi$. Also, $\text{div}\mathbf{B}$ yields $\nabla^2\varphi = 0$. Then, we get

$$\epsilon_{\text{out}} = \frac{1}{2\mu_0} \int d\mathbf{S}_{\text{out}} \cdot (\varphi\nabla\varphi). \tag{A4}$$

Here, $B^2 = (\nabla\varphi)^2 = \nabla \cdot (\varphi\nabla\varphi)$ is used. Next, we calculate ϵ_{in} using the Maxwell-London equation in an inhomogeneous superconductor, $\mathbf{B} + \mu_0\text{rot}(\lambda^2\mathbf{j}) = 0$ or

$$\mathbf{B} + \lambda^2\text{rot}\,\text{rot}\mathbf{B} + (\nabla\lambda^2) \times \text{rot}\mathbf{B} = 0, \tag{A5}$$

which is valid outside the vortex core. We find the following relation:

$$\begin{aligned}
\nabla \cdot &[(\lambda^2\mathbf{B}) \times \text{rot}\mathbf{B}] \\
&= \text{rot}\mathbf{B} \cdot \text{rot}(\lambda^2\mathbf{B}) - (\text{rot}\,\text{rot}\mathbf{B}) \cdot (\lambda^2\mathbf{B}) \\
&= \text{rot}\mathbf{B} \cdot \text{rot}(\lambda^2\mathbf{B}) + B^2 + [(\nabla\lambda^2) \times \text{rot}\mathbf{B}] \cdot \mathbf{B} \\
&= \lambda^2(\text{rot}\mathbf{B})^2 + B^2 = \mu_0^2\lambda^2 j^2 + B^2.
\end{aligned} \tag{A6}$$

Here, Eq. (A5) is used from the second line to the third line, and $\text{rot}\mathbf{B} = \mu_0\mathbf{j}$ is used in the last line. Hence, ϵ_{in} can be written as

$$\epsilon_{\text{in}} = \frac{1}{2\mu_0} \int d\mathbf{S}_{\text{in}} \cdot [(\lambda^2\mathbf{B}) \times \text{rot}\mathbf{B}] = \epsilon_{\text{in}}^{(C)} + \epsilon_{\text{in}}^{(V)}. \tag{A7}$$

Here, $\epsilon_{\text{in}}^{(C)}$ and $\epsilon_{\text{in}}^{(V)}$ are the contributions from the core surface and the vacuum-superconductor interface, respectively:

$$\epsilon_{\text{in}}^{(C)} = \frac{1}{2} \int d\mathbf{S}_{\text{in}}^{(C)} \cdot [(\lambda^2\mathbf{B}) \times \mathbf{j}], \tag{A8}$$

$$\begin{aligned}
\epsilon_{\text{in}}^{(V)} &= \frac{1}{2} \int d\mathbf{S}_{\text{in}}^{(V)} \cdot [(\lambda^2\nabla\varphi) \times \mathbf{j}] \\
&= -\frac{1}{2} \int d\mathbf{S}_{\text{in}}^{(V)} \cdot [(\nabla\lambda^2) \times \mathbf{j} + \lambda^2\text{rot}\mathbf{j}]\varphi. \tag{A9}
\end{aligned}$$

In the last line, $\text{rot}(\lambda^2\varphi\mathbf{j}) = \nabla((\lambda^2\varphi) \times \mathbf{j} + (\lambda^2\varphi\text{rot}\mathbf{j}$ and $\nabla((\lambda^2\varphi) = \lambda^2\nabla\varphi + \varphi(\nabla\lambda^2)$ are used. Using $d\mathbf{S}_{\text{in}}^{(V)} =$

$-d\mathbf{S}_{\mathrm{out}}$, Eq. (A1) results in

$$
\begin{aligned}
\epsilon &= \epsilon_{\mathrm{out}} + \epsilon_{\mathrm{in}} \\
&= \frac{1}{2\mu_0} \int d\mathbf{S}_{\mathrm{out}} \cdot [\mathbf{B} + (\nabla\lambda^2) \\
&\quad \times \mathrm{rot}\mathbf{B} + \lambda^2 \mathrm{rot}\,\mathrm{rot}\mathbf{B}]\varphi + \epsilon_{\mathrm{in}}^{(C)} \\
&= \frac{\phi_0}{2\mu_0}[\varphi(\mathbf{r}_{\mathrm{ent}}) - \varphi(\mathbf{r}_{\mathrm{ex}})] + \epsilon_{\mathrm{in}}^{(C)}
\end{aligned}
\tag{A10}
$$

$\varphi(\mathbf{r}_{\mathrm{ent}})$ and $\varphi(\mathbf{r}_{\mathrm{ex}})$ represent the potentials at the points where the vortex enters and exits, respectively.

Now, let us consider thin films positioned on the x-y plane. In the case of a thin film, we can neglect $\epsilon_{\mathrm{in}}^{(C)}$, resulting in the following simplified expression:

$$
\epsilon = -\frac{\phi_0}{\mu_0}\varphi(\mathbf{r}_{\mathrm{ex}}).
\tag{A11}
$$

Integrating $\mu_0 \mathbf{j} = \mathrm{rot}\,\mathbf{B}$ over the film thickness, we get

$$
J_x = -\frac{2}{\mu_0}B_y(+0) = -\frac{2}{\mu_0}\partial_y\varphi(+0),
\tag{A12}
$$

$$
J_y = \frac{2}{\mu_0}B_x(+0) = \frac{2}{\mu_0}\partial_x\varphi(+0).
\tag{A13}
$$

On the other hand, we have the relations $J_x = \partial_y\Psi$ and $J_y = -\partial_x\Psi$. We get $\varphi(+0) = -(\mu_0/2)\Psi$. Then, finally we get

$$
\epsilon = \frac{\phi_0}{2}\Psi(\mathbf{r}_v),
\tag{A14}
$$

which corresponds to the formula derived by Kogan for a homogeneous film.

APPENDIX B: IMPLEMENT A PEARL-LENGTH INHOMOGENEITY VIA DOPING NONMAGNETIC IMPURITIES

1. Pearl-length inhomogeneity and impurity distribution

Here, we explore the process of inducing inhomogeneity in the Pearl length $\Lambda = 2\lambda^2/d$ by controlling the London length λ. One of the simplest approaches to achieve this is by doping nonuniform nonmagnetic impurities. In the case of a dirty limit superconductor, the London length is given by (see, e.g., Refs. [6,29])

$$
\lambda(x) = \lambda_{\mathrm{clean}}\sqrt{\frac{\xi_0}{\ell(x)}} = \lambda_{\mathrm{clean}}\sqrt{\frac{2\Gamma_{\mathrm{imp}}(x)}{\pi\Delta_0}}.
\tag{B1}
$$

Here, λ_{clean} represents the clean-limit London length, $\xi_0 = \hbar v_f/\pi\Delta_0$ is the BCS coherence length, $\ell = v_f\tau$ is the

mean free path, τ denotes the electron relaxation time, v_f is the Fermi velocity, Δ_0 stands for the zero-temperature BCS pair potential, and $\Gamma_{\mathrm{imp}} = \hbar/2\tau$ represents the nonmagnetic impurity scattering rate. Notably, Δ_0 remains unaffected by the concentration of nonmagnetic impurities and remains independent of x. Then, we find

$$
\Lambda(x) = \Lambda_{\mathrm{clean}}\frac{2\Gamma_{\mathrm{imp}}(x)}{\pi\Delta_0}.
\tag{B2}
$$

Here, $\Lambda_{\mathrm{clean}} = 2\lambda_{\mathrm{clean}}^2/d$ represents the clean-limit Pearl length. By introducing $\Lambda_0 = \Lambda(0)$, we can express the relationship as

$$
\frac{\Lambda(x)}{\Lambda_0} = \frac{\Gamma_{\mathrm{imp}}(x)}{\Gamma_{\mathrm{imp}}(0)} = \frac{n_{\mathrm{imp}}(x)}{n_{\mathrm{imp}}(0)}.
\tag{B3}
$$

Here, n_{imp} is the concentration of nonmagnetic impurities.

2. Low-temperature bake of superconducting circuit

To achieve a desired impurity distribution $n_{\mathrm{imp}}(x)/n_{\mathrm{imp}}(0)$ in superconducting thin-film strips, we can explore the utilization of the low-temperature bake (LTB) technique commonly employed in Nb cavity fabrication within the superconducting particle accelerator community. The LTB process is known to diffuse oxygen from the natural oxide layer to the bulk of the Nb cavity. By incorporating the LTB process into the fabrication of superconducting thin-film strips, we can potentially tailor the desired inhomogeneous Pearl-length distribution, including both left-right symmetric and left-right asymmetric Pearl-length distributions.

The process of patterning a superconducting circuit, which includes the incorporation of the LTB process to achieve a left-right *symmetric* impurity distribution, can be outlined as follows (see Fig. 10). (i) Deposit Nb material onto the substrate using techniques like sputtering and spin coat a layer of photoresist onto the Nb film. (ii) Expose the photoresist-coated substrate to UV light through a mask containing the circuit pattern and develop the photoresist using a developer solution. (iii) Etch away the underlying Nb material, leaving the desired circuit pattern on the remaining Nb film. (iv) Expose the Nb film to air, forming a natural oxide layer on the sides of the circuit. Then, place the circuit into an ultrahigh vacuum chamber and bake it at a specific temperature T_{bake} for a duration of τ_{bake}. (v) Strip away the remaining photoresist, leaving behind the thin-film strip with a left-right symmetric impurity distribution.

A possible method to make a left-right *asymmetric* impurity distribution can be outlined as follows (see Fig. 10): (I) Follow steps (i)–(iv). (II) Spin coat a layer of photoresist. (III) Expose the photoresist-coated substrate to UV light through the mask shifted slightly and develop the photoresist using a developer solution. (IV) Etch away
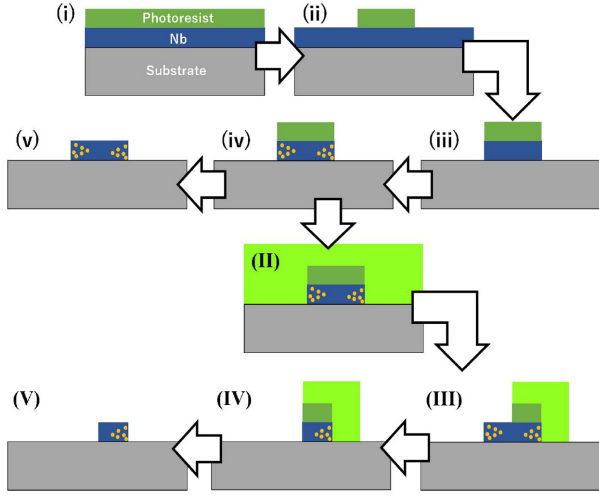
FIG. 10. Schematic representations of possible fabrication schemes to achieve left-right symmetric and asymmetric impurity distributions in superconducting thin-film strips utilizing the low-temperature bake. The orange dots represent oxygen diffused from the left and right edges, contributing to the desired impurity distribution.

the underlying Nb material, leaving the Nb strip with half width. (V) Strip away the remaining photoresist, leaving behind the thin-film strip with a left-right asymmetric impurity distribution.

In the conventional process of patterning a superconducting circuit, steps (i)–(iii) and (v) are typically performed. However, in this modified procedure, we introduce step (iv): the LTB process. The traditional recipe for a particle accelerator cavity uses $(T_{\text{bake}}, \tau_{\text{bake}}) = (120\,^\circ\text{C}, 48\,\text{h})$, which allows oxygen to infuse to a depth of $\delta_{\text{bake}} =$ 10–100 nm from the left and right edges of the thin-film strip. However, this combination of $(T_{\text{bake}}, \tau_{\text{bake}})$ may not be optimal for our purpose. Determining the optimum combination of T_{bake} and τ_{bake} requires experiments and simulations of the diffusion equation, which are beyond the scope of this paper. The oxygen profile for a general $(T_{\text{bake}}, \tau_{\text{bake}})$ can be obtained by solving the diffusion equation, taking into account both the diffusion of oxygen initially distributed at the edges and the diffusion of oxygen provided by the reduction of oxide [17,21]. Calculation results will be presented elsewhere.

APPENDIX C: DERIVATIONS OF $I_{\text{V, AV}}^{(\pm)}$

The vortex-entry current I_{V} (or antivortex-entry current I_{AV}) represents the current at which the edge barrier vanishes. This condition can be expressed as $G(X_p; I_{\text{V, AV}}) = 0$, where X_p denotes the peak position of the edge barrier, satisfying $G'(X_p; I_{\text{V, AV}}) = 0$.

To get $I_{\text{V}}^{(+)}$ and $I_{\text{AV}}^{(-)}$, we expand $G(X)$ around the left edge $X/W = -1/2 + \delta$ ($\delta \ll 1$). We find

$$\frac{G(X)}{\epsilon_0} = \frac{1}{F(-W/2)}\left[\ln\frac{2\delta}{\xi_L/W} \mp (\tilde{B}_L + \tilde{I})\delta\right] \quad (C1)$$

for a vortex (an antivortex) in the current $I \geq 0$ ($I \leq 0$). To get $I_{\text{V}}^{(-)}$ and $I_{\text{AV}}^{(+)}$, we expand $G(X)$ around the right edge $X/W = 1/2 - \delta$. We find

$$\frac{G(X)}{\epsilon_0} = \frac{1}{F(W/2)}\left[\ln\frac{2\delta}{\xi_R/W} \pm (\tilde{B}_R + \tilde{I})\delta\right] \quad (C2)$$

for a vortex (an antivortex) in the current $I \leq 0$ ($I \geq 0$). Here, $\tilde{I}$ and $\tilde{B}_{L,R}$ are given as follows.

For a homogeneous film ($F = 1$ and $\xi_L = \xi_R = \xi$), we have

$$\tilde{I} = \frac{I}{I_0}, \quad (C3)$$

$$\tilde{B}_{L,R} = \pm\frac{4B}{B_\phi}. \quad (C4)$$

For an inhomogeneous film with a quadratic distribution of Λ (see Fig. 5), we have

$$\tilde{I} = \frac{I}{I_0}\frac{4 - \gamma}{4}\frac{\sqrt{\gamma/(4 - \gamma)}}{\tan^{-1}\sqrt{\gamma/(4 - \gamma)}}, \quad (C5)$$

$$\tilde{B}_{L,R} = \pm\frac{4B}{B_\phi}. \quad (C6)$$

For an inhomogeneous film with a left-right asymmetric distribution of Λ (see Fig. 8), we have

$$\tilde{I} = \frac{I}{I_0}\frac{2\alpha}{\ln[(1 + \alpha)/(1 - \alpha)]}, \quad (C7)$$

$$\tilde{B}_{L,R} = \frac{2(B/B_\phi)}{\alpha\tanh^{-1}\alpha}\left(2\alpha - (1 \mp \alpha)\ln\frac{1 + \alpha}{1 - \alpha}\right). \quad (C8)$$

Note that, taking $\gamma \to 0$ and $\alpha \to 0$, we can reproduce the results for the homogeneous case from the inhomogeneous cases.

The condition of the disappearance of the edge barrier yields

$$\tilde{I}_{\text{V}}^{(\pm)} = \frac{2W}{e\xi_{L,R}} \mp \tilde{B}_{L,R}, \quad (C9)$$

$$\tilde{I}_{\text{AV}}^{(\pm)} = \frac{2W}{e\xi_{R,L}} \mp \tilde{B}_{R,L}, \quad (C10)$$

which immediately yield Eqs. (45) and (46), Eqs. (53) and (54), and Eqs. (62) and (63).
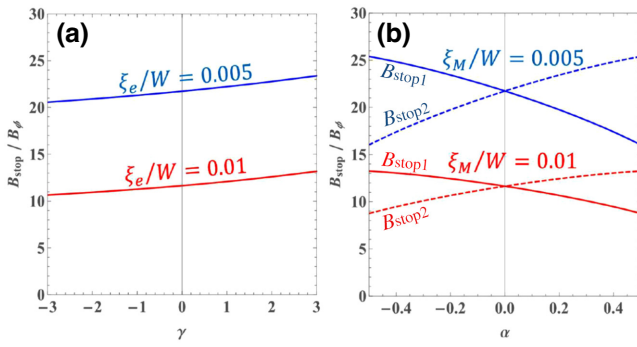
FIG. 11. B_{stop} of inhomogeneous narrow thin-film strips as a function of the inhomogeneity parameter. (a) Quadratic distribution of $\Lambda(x)$ (see Fig. 3). The coherence length at the edges is denoted as $\xi_e = \xi|x = \pm W/2$. (b) Left-right asymmetric distribution of $\Lambda(x)$ (see Fig. 8). Here, we consider the inhomogeneity to arise from variations in impurity concentration. In this case, the coherence length at the edges can be calculated as $\xi_L = \xi_M/F(-W/2) = \xi_M/\sqrt{1-\alpha}$ and $\xi_R = \xi_M/F(W/2) = \xi_M/\sqrt{1+\alpha}$, where $\xi_M = \xi|_{x=0}$ is the coherence length at the middle of the strip.

APPENDIX D: B_{stop} IN INHOMOGENEOUS FILMS

As discussed in Sec. III A, the linear dependence of I_c on B breaks down when $B \gtrsim B_{\text{stop}}$. At this critical magnetic field value, a free-energy minimum appears at a point X_s where $G'(X_s; I_c, B_{\text{stop}}) = 0$, and vortices come to a stop at this minimum [66,67]. These vortices, carrying a current, then impact the barrier and modify the behavior of I_c.

The critical value B_{stop} is determined by the condition for the existence of a solution X_s that satisfies $G'(X_s; I_c, B_{\text{stop}}) = 0$. For a film with a quadratic distribution of $\Lambda(x)$ (as shown in Fig. 3), we analyze this condition using the expression of G given by Eq. (52). The dependence of B_{stop} on γ is illustrated in Fig. 11(a). Moreover, when the film is homogeneous ($\gamma = 0$), the calculated value of B_{stop} coincides with the result obtained from Eq. (48).

On the other hand, for a film with a left-right asymmetric distribution of $\Lambda(x)$ (as depicted in Fig. 8), we consider the condition using G given by Eq. (61), resulting in two distinct critical values: $B_{\text{stop}1}$ and $B_{\text{stop}2}$ for penetration from the left edge and right edge, respectively. The linear dependence on B holds within the ranges $-B_{\text{stop}2} < B < B_{\text{stop}1}$ for $I_c^{(+)}$ and $-B_{\text{stop}1} < B < B_{\text{stop}2}$ for $I_c^{(-)}$.

[1] E. Grumbling and M. Horowitz, *Quantum Computing: Progress And Prospects* (The National Academy Press, Washington, DC, 2019).

[2] T. M. Klapwijk and A. V. Semenov, Engineering physics of superconducting hot-electron bolometer mixers, IEEE Trans. Terahertz Sci. Technol. **7**, 627 (2017).

[3] J. Zmuidzinas and P. L. Richards, Superconducting detectors and mixers for millimeter and submillimeter astrophysics, Proc. IEEE **92**, 1597 (2004).

[4] J. Zmuidzinas, Superconducting Microresonators: Physics and Applications, Annu. Rev. Condens. Matter Phys. **3**, 169 (2012).

[5] H. Padamsee, 50 years of success for SRF accelerators-a review, Supercond. Sci. Technol. **30**, 053003 (2017).

[6] A. Gurevich, Theory of RF superconductivity for resonant cavities, Supercond. Sci. Technol. **30**, 034004 (2017).

[7] A. Grassellino, A. Romanenko, D. Sergatskov, O. Melnychuk, Y. Trenikhina, A. Crawford, A. Rowe, M. Wong, T. Khabiboulline, and F. Barkov, Nitrogen and argon doping of niobium for superconducting radio frequency cavities: A pathway to highly efficient accelerating structures, Supercond. Sci. Technol. **26**, 102001 (2013).

[8] P. Dhakal, G. Ciovati, G. R. Myneni, K. E. Gray, N. Groll, P. Maheshwari, D. M. McRae, R. Pike, T. Proslier, and F. Stevie, *et al.*, Effect of high temperature heat treatments on the quality factor of a large-grain superconducting radiofrequency niobium cavity, Phys. Rev. ST Accel. Beams **16**, 042001 (2013).

[9] A. Grassellino, A. Romanenko, Y. Trenikhina, M. Checchin, M. Martinello, O. S. Melnychuk, S. Chandrasekaran, D. A. Sergatskov, S. Posen, and A. C. Crawford, *et al.*, Unprecedented quality factors at accelerating gradients up to 45 MVm^{-1} in niobium superconducting resonators via low temperature nitrogen infusion, Supercond. Sci. Technol. **30**, 094004 (2017).

[10] P. Dhakal, S. Chetri, S. Balachandran, P. J. Lee, and G. Ciovati, Effect of low temperature baking in nitrogen on the performance of a niobium superconducting radio frequency cavity, Phys. Rev. Accel. Beams **21**, 032001 (2018).

[11] T. Konomi, T. Dohmae, Y. Hori, E. Kako, T. Kubo, G. T. Park, H. Sakai, K. Umemori, J. Kamiya, K. Takeishi, and T. Nagata, in *Proceedings of SRF2017, Lanzhou, China* (JACoW, CERN, Geneva, 2017), p. 775.

[12] E. M. Lechner, B. D. Oli, J. Makita, G. Ciovati, A. Gurevich, and M. Iavarone, Electron Tunneling and X-Ray Photoelectron Spectroscopy Studies of the Superconducting Properties of Nitrogen-Doped Niobium Resonator Cavities, Phys. Rev. Appl. **13**, 044044 (2020).

[13] A. Romanenko, R. Pilipenko, S. Zorzetti, D. Frolov, M. Awida, S. Belomestnykh, S. Posen, and A. Grassellino, Three-Dimensional Superconducting Resonators at $T < 20$ mK with Photon Lifetimes up to $\tau = 2$ s, Phys. Rev. Appl. **13**, 034032 (2020).

[14] S. Posen, A. Romanenko, A. Grassellino, O. S. Melnychuk, and D. A. Sergatskov, Ultralow Surface Resistance via Vacuum Heat Treatment of Superconducting Radio-Frequency Cavities, Phys. Rev. Appl. **13**, 014024 (2020).

[15] H. Ito, H. Araki, K. Takahashi, and K. Umemori, Influence of furnace baking on Q-E behavior of superconducting accelerating cavities, Prog. Theor. Exp. Phys. **2021**, 071G01 (2021).

[16] F. He, W. Pan, P. Sha, J. Zhai, Z. Mi, X. Dai, S. Jin, Z. Zhang, C. Dong, B. Liu, *et al.*, Medium-temperature furnace baking of 1.3 GHz 9-cell superconducting cavities at IHEP, Supercond. Sci. Technol. **34**, 095005 (2021).

[17] E. M. Lechner, J. W. Angle, F. A. Stevie, M. J. Kelley, C. E. Reece, and A. D. Palczewski, RF surface resistance tuning

of superconducting niobium via thermal diffusion of native oxide, Appl. Phys. Lett. **119,** 082601 (2021).

[18] M. Wenskat, J. Čížek, M. O. Liedke, M. Butterling, M. Stiehl, G. D. L. Semione, C. Backes, C. Bate, O. Melikhova, E. Hirschmann, A. Wagner, H. Weise, A. Stierle, M. Aeschlimann, and W. Hillert, Vacancy dynamics in niobium and its native oxides and their potential implications for quantum computing and superconducting accelerators, Phys. Rev. B **106,** 094516 (2022).

[19] K. Saito, H. Inoue, E. Kako, T. Fujino, S. Noguchi, M. Ono, and T. Shishido, in *Proceedings of SRF1997, Abano Terme, Padova, Italy* (JACoW, CERN Geneva, 1997), p. 795.

[20] L. Lilje, D. Reschke, K. Twarowski, P. Schmuser, D. Bloess, E. Chiaveri, E. Haebel, H. Preis, J.-M. Tessier, H. Wenninger, J. P. Charrier, and H. Safa, in *Proceedings of SRF1999, La Fonda Hotel, Santa Fe, New Mexico, USA* (JACoW, CERN Geneva, 1999), p. 74.

[21] G. Ciovati, Improved oxygen diffusion model to explain the effect of low-temperature baking on high field losses in niobium superconducting cavities, Appl. Phys. Lett. **89,** 022507 (2006).

[22] R. L. Geng, G. V. Eremeev, H. Padamsee, and V. D. Shemelin, in *Proceedings of PAC07, Albuquerque, New Mexico, USA* (JACoW, CERN Geneva, 2007), p. 2337.

[23] T. Kubo, Y. Ajima, H. Inoue, K. Umemori, Y. Watanabe, and M. Yamanaka, in *Proceedings of IPAC2014, Dresden, Germany* (JACoW, CERN Geneva, 2014), p. 2519.

[24] K. Maki, On persistent currents in a superconducting alloy I, Prog. Theor. Phys. **29,** 10 (1963).

[25] M. Yu Kupriyanov and V. F. Lukichev, Temperature dependence of pair-breaking current in superconductors, Fiz. Nizk. Temp. **6,** 445 (1980).

[26] F. Pei-Jen and A. Gurevich, Effect of impurities on the superheating field of type-II superconductors, Phys. Rev. B **85,** 054513 (2012).

[27] T. Kubo, Weak-field dissipative conductivity of a dirty superconductor with Dynes subgap states under a dc bias current up to the depairing current density, Phys. Rev. Res. **2,** 013302 (2020).

[28] T. Kubo, Superfluid flow in disordered superconductors with Dynes pair-breaking scattering: Depairing current, kinetic inductance, and superheating field, Phys. Rev. Res. **2,** 033203 (2020).

[29] T. Kubo, Effects of Nonmagnetic Impurities and Subgap States on the Kinetic Inductance, Complex Conductivity, Quality Factor, and Depairing Current Density, Phys. Rev. Appl. **17,** 014018 (2022).

[30] A. Gurevich, Enhancement of rf breakdown field of superconductors by multilayer coating, Appl. Phys. Lett. **88,** 012511 (2006).

[31] T. Kubo, Y. Iwashita, and T. Saeki, Radio-frequency electromagnetic field and vortex penetration in multilayered superconductors, Appl. Phys. Lett. **104,** 032603 (2014).

[32] A. Gurevich, Maximum screening fields of superconducting multilayer structures, AIP Adv. **5,** 017112 (2015).

[33] D. B. Liarte, S. Posen, M. K. Transtrum, G. Catelani, M. Liepe, and J. P. Sethna, Theoretical estimates of maximum fields in superconducting resonant radio frequency cavities: Stability theory, disorder, and laminates Supercond. Sci. Technol. **30,** 033002 (2017).

[34] T. Kubo, Multilayer coating for higher accelerating fields in superconducting radio-frequency cavities: A review of theoretical aspects, Supercond. Sci. Technol. **30,** 023001 (2017).

[35] V. Ngampruetikorn and J. A. Sauls, Effect of inhomogeneous surface disorder on the superheating field of superconducting RF cavities, Phys. Rev. Res. **1,** 012015(R) (2019).

[36] T. Kubo, Superheating fields of semi-infinite superconductors and layered superconductors in the diffusive limit: Structural optimization based on the microscopic theory, Supercond. Sci. Technol. **34,** 045006 (2021).

[37] T. Tan, M. A. Wolak, X. X. Xi, T. Tajima, and L. Civale, Magnesium diboride coated bulk niobium: A new approach to higher acceleration gradient, Sci. Rep. **6,** 35879 (2016).

[38] A.-M. Valente-Feliciano, Superconducting RF materials other than bulk niobium: A review, Supercond. Sci. Technol. **29,** 113002 (2016).

[39] C. Z. Antoine, M. Aburas, A. Four, F. Weiss, Y. Iwashita, H. Hayano, S. Kato, T. Kubo, and T. Saeki, Optimization of tailored multilayer superconductors for RF application and protection against premature vortex penetration, Supercond. Sci. Technol. **32,** 085005 (2019).

[40] H. Ito, C. Z. Antoine, H. Hayano, R. Katayama, T. Kubo, T. Saeki, R. Ito, T. Nagata, Y. Iwashita, and H. Tongu, in *Proceedings of SRF2019, Dresden, Germany* (JACoW, CERN Geneva, 2019), p. 632.

[41] R. Katayama, H. Hayano, T. Kubo, T. Saeki, C. Z. Antoine, H. Ito, R. Ito, Y. Iwashita, H. Tongu, and T. Nagata, in *Proceedings of SRF2019, Dresden, Germany* (JACoW, CERN Geneva, 2019), p. 807.

[42] Z. Lin, M. Qin, D. Li, P. Shen, L. Zhang, Z. Feng, P. Sha, J. Miao, J. Yuan, and X. Dong, *et al.*, Enhancement of the lower critical field in FeSe-coated Nb structures for superconducting radio-frequency applications, Supercond. Sci. Technol. **34,** 015001 (2021).

[43] A.-M. Valente-Feliciano, C. Antoine, S. Anlage, G. Ciovati, J. Delayen, F. Gerigk, A. Gurevich, T. Junginger, S. Keckert, G. Keppe, *et al.*, in *Proceedings of the 2021 US Community Study on the Future of Particle Physics (Snowmass 2021), WA, USA* (APS Division of Particles and Fields, MD, USA, 2022), https://www.slac.stanford.edu/econf/C210711/.

[44] K. K. Likharev, The formation of a mixed state in planar semiconductor films, Radiophys. Quantum Electron. **6,** 722 (1972).

[45] G. Stan, S. B. Field, and J. M. Martinis, Critical Field for Complete Vortex Expulsion from Narrow Superconducting Strips Phys. Rev. Lett. **92,** 097003 (2004).

[46] E. Bronson, M. P. Gelfand, and S. B. Field, Equilibrium configurations of Pearl vortices in narrow strips, Phys. Rev. B **73,** 144501 (2006).

[47] L. N. Bulaevskii, M. J. Graf, and V. G. Kogan, Vortex-assisted photon counts and their magnetic field dependence in single-photon superconducting detectors, Phys. Rev. B **85,** 014505 (2012).

[48] D. Y. Vodolazov and F. M. Peeters, Superconducting rectifier based on the asymmetric surface barrier effect, Phys. Rev. B **72,** 172508 (2005).

[49] Y. Hou, F. Nichele, H. Chi, A. Lodesani, Y. Wu, M. F. Ritter, D. Z. Haxell, M. Davydova, S. Ilic, F. S. Bergeret, A. Kamra, L. Fu, P. A. Lee, and J. S. Moodera, Ubiquitous Superconducting Diode Effect in Superconductor Thin Films, Phys. Rev. Lett. **131**, 027001 (2023).

[50] D. Suri, A. Kamra, T. N. G. Meier, M. Kronseder, W. Belzig, C. H. Back, and C. Strunk, Non-reciprocity of vortex-limited critical current in conventional superconducting micro-bridges, Appl. Phys. Lett. **121**, 102601 (2022).

[51] R. Wakatsuki and N. Nagaosa, Nonreciprocal Current in Noncentrosymmetric Rashba Superconductors, Phys. Rev. Lett. **121**, 026601 (2018).

[52] F. Ando, Y. Miyasaka, T. Li, J. Ishizuka, T. Arakawa, Y. Shiota, T. Moriyama, Y. Yanase, and T. Ono, Observation of superconducting diode effect, Nature **584**, 373 (2020).

[53] H. Wu, Y. Wang, Y. Xu, P. K. Sivakumar, C. Pasco, U. Filippozzi, S. S. P. Parkin, Y.-J. Zeng, T. McQueen, and M. N. Ali, The field-free Josephson diode in a van der Waals heterostructure, Nature **604**, 653 (2022).

[54] A. Daido, Y. Ikeda, and Y. Yanase, Intrinsic Superconducting Diode Effect, Phys. Rev. Lett. **128**, 037001 (2022).

[55] N. F. Q. Yuan and L. Fu, Supercurrent diode effect and finite-momentum superconductors, Proc. Natl Acad. Sci. USA **119**, e2119548119 (2022).

[56] S. Ilic and F. S. Bergeret, Theory of the Supercurrent Diode Effect in Rashba Superconductors with Arbitrary Disorder, Phys. Rev. Lett. **128**, 177001 (2022).

[57] T. Karabassov, I. V. Bobkova, A. A. Golubov, and A. S. Vasenko, Hybrid helical state and superconducting diode effect in superconductor/ferromagnet/topological insulator heterostructures, Phys. Rev. B **106**, 224509 (2022).

[58] L. Bauriedl, C. Bäuml, L. Fuchs, C. Baumgartner, N. Paulik, J. M. Bauer, K.-Q. Lin, J. M. Lupton, T. Taniguchi, K. Watanabe, *et al.*, Supercurrent diode effect and magnetochiral anisotropy in few-layer **NbSe**$_2$, Nat. Commun. **13**, 4266 (2022).

[59] A. Yu. Aladyshkin, A. S. Mel'nikov, I. A. Shereshevsky, and I. D. Tokman, What is the best gate for vortex entry into type-II superconductor, Physica C **361**, 67 (2001).

[60] J. R. Clem and K. K. Berggren, Geometry-dependent critical currents in superconducting nanocircuits, Phys. Rev. B **84**, 174510 (2011).

[61] T. Kubo, Field limit and nano-scale surface topography of superconducting radio-frequency cavity made of extreme type II superconductor, Prog. Theor. Exp. Phys. **2015**, 063G01 (2015).

[62] G. M. Maksimova, Mixed state and critical current in narrow semiconducting films, Phys. Solid State **40**, 1607 (1998).

[63] V. G. Kogan, Pearl's vortex near the film edge, Phys. Rev. B **49**, 15874 (1994).

[64] J. R. Clem, Vortex exclusion from superconducting strips and SQUIDs in weak perpendicular ambient magnetic fields, Bull. Amer. Phys. Soc. **43**, 401 (1998).

[65] V. G. Kogan, Interaction of vortices in thin superconducting films and the Berezinskii-Kosterlitz-Thouless transition, Phys. Rev. B **75**, 064514 (2007).

[66] J. R. Clem, Y. Mawatari, G. R. Berdiyorov, and F. M. Peeters, Predicted field-dependent increase of critical currents in asymmetric superconducting nanocircuits, Phys. Rev. B **85**, 144511 (2012).

[67] K. Ilin, D. Henrich, Y. Luck, Y. Liang, M. Siegel, and D. Yu. Vodolazov, Critical current of Nb, NbN, and TaN thin-film bridges with and without geometrical nonuniformities in a magnetic field, Phys. Rev. B **89**, 184511 (2014).

[68] V. G. Kogan and M. Ichioka, Vortex cores in narrow thin-film strips, J. Phys. Soc. Jpn. **89**, 094711 (2020).

[69] F. Tafuri, J. R. Kirtley, D. Born, D. Stornaiuolo, P. G. Medaglia, P. Orgiani, G. Balestrino, and V. G. Kogan, Dissipation in ultra-thin current-carrying superconducting bridges; evidence for quantum tunneling of Pearl vortices, Europhys. Lett. **73**, 948 (2006).

[70] J. R. Cave and J. E. Evetts, Critical temperature profile determination using a modified London equation for inhomogeneous superconductors, J. Low Temp. Phys. **63**, 35 (1986).

[71] A. Romanenko, A. Grassellino, A. C. Crawford, D. A. Sergatskov, and O. Melnychuk, Ultra-high quality factors in superconducting niobium cavities in ambient magnetic fields up to 190 mG, Appl. Phys. Lett. **105**, 234103 (2014).

[72] S. Huang, T. Kubo, and R. L. Geng, Dependence of trapped-flux-induced surface resistance of a large-grain Nb superconducting radio-frequency cavity on spatial temperature gradient during cooldown through T_c, Phys. Rev. Accel. Beams **19**, 082001 (2016).

[73] S. Posen, M. Checchin, A. C. Crawford, A. Grassellino, M. Martinello, O. S. Melnychuk, A. Romanenko, D. A. Segatskov, and Y. Trenikhina, Efficient expulsion of magnetic flux in superconducting radio frequency cavities for high Q applications, J. Appl. Phys. **119**, 213903 (2016).

[74] D. Longuevergne and A. Miyazaki, Impact of geometry on the magnetic flux trapping of superconducting accelerating cavities, Phys. Rev. Accel. Beams **24**, 083101 (2021).

[75] S. Ooi, M. Tachiki, T. Konomi, T. Kubo, A. Kikuchi, S. Arisawa, H. Ito, and K. Umemori, Observation of intermediate mixed state in high-purity cavity-grade Nb by magneto-optical imaging, Phys. Rev. B **104**, 064504 (2021).

[76] D. C. Mattis and J. Bardeen, Theory of the anomalous skin effect in normal and superconducting metals, Phys. Rev. **111**, 412 (1958).

[77] A. A. Abrikosov, L. P. Gor'kov, and I. M. Khalatnikov, A superconductor in a high frequency field, J. Exp. Theor. Phys. **35**, 265 (1958).

[78] Y. V. Fominov, M. Houzet, and L. I. Glazman, Surface impedance of superconductors with weak magnetic impurities, Phys. Rev. B **84**, 224517 (2011).

[79] M. Kharitonov, T. Proslier, A. Glatz, and M. J. Pellin, Surface impedance of superconductors with magnetic impurities, Phys. Rev. B **86**, 024514 (2012).

[80] J. R. Clem and V. G. Kogan, Kinetic impedance and depairing in thin and narrow superconducting films, Phys. Rev. B **86**, 174521 (2012).

[81] A. Gurevich, Reduction of Dissipative Nonlinear Conductivity of Superconductors by Static and Microwave Magnetic Fields, Phys. Rev. Lett. **113**, 087001 (2014).

[82] A. V. Semenov, I. A. Devyatov, P. J. de Visser, and T. M. Klapwijk, Coherent Excited States in Superconductors due to a Microwave Field, Phys. Rev. Lett. **117**, 047002 (2016).

[83] A. Gurevich and T. Kubo, Surface impedance and optimum surface resistance of a superconductor with an imperfect surface, Phys. Rev. B **96,** 184515 (2017).

[84] F. Herman and R. Hlubina, Microwave response of superconductors that obey local electrodynamics, Phys. Rev. B **104,** 094519 (2021).

[85] T. Kubo and A. Gurevich, Field-dependent nonlinear surface resistance and its optimization by surface nanostructuring in superconductors, Phys. Rev. B **100,** 064522 (2019).

[86] A. Gurevich, T. Kubo, and J. A. Sauls, in *Proceedings of the 2021 US Community Study on the Future of Particle Physics (Snowmass 2021), WA, USA* (APS Division of Particles and Fields, MD, USA, 2022), https://www.slac.stanford.edu/econf/C210711/.

[87] P. J. de Visser, J. J. A. Baselmans, S. J. C. Yates, P. Diener, A. Endo, and T. M. Klapwijk, Microwave-induced excess quasiparticles in superconducting resonators measured through correlated conductivity fluctuations, Appl. Phys. Lett. **100,** 162601 (2012).

[88] P. J. de Visser, D. J. Goldie, P. Diener, S. Withington, J. J. A. Baselmans, and T. M. Klapwijk, Evidence of a Nonequilibrium Distribution of Quasiparticles in the Microwave Response of a Superconducting Aluminum Resonator, Phys. Rev. Lett. **112,** 047004 (2014).

[89] T. Guruswamy, D. J. Goldie, and S. Withington, Nonequilibrium superconducting thin films with sub-gap and pair-breaking photon illumination, Supercond. Sci. Technol. **28,** 054002 (2015).

[90] R. Barends, J. J. A. Baselmans, S. J. C. Yates, J. R. Gao, J. N. Hovenier, and T. M. Klapwijk, Quasiparticle Relaxation in Optically Excited High-Q Superconducting Resonators, Phys. Rev. Lett. **100,** 257002 (2008).

[91] M. Naruse, Y. Sekimoto, T. Noguchi, A. Miyachi, T. Nitta, and Y. Uzawa, Development of crystal Al MKIDs by molecular beam epitaxy, J. Low Temp. Phys. **167,** 373 (2012).

[92] T. Kubo, An encouraging of paternity leave: A physicist who has become a stay-at-home dad in New York, J. Part. Accel. Soc. Jpn. **20,** 50 (2023).